Aalto University

OPEN ACCESS

This is an electronic reprint of the original article.
This reprint may differ from the original in pagination and typographic detail.

Abed, Ayman A.; Sołowski, Wojciech T.

A study on how to couple thermo-hydro-mechanical behaviour of unsaturated soils: Physical equations, numerical implementation and examples

Published in:
Computers and Geotechnics

DOI:
10.1016/j.compgeo.2017.07.021

Published: 01/12/2017

Document Version
Publisher's PDF, also known as Version of record

Published under the following license:
CC BY-NC-ND

Please cite the original version:
Abed, A. A., & Sołowski, W. T. (2017). A study on how to couple thermo-hydro-mechanical behaviour of unsaturated soils: Physical equations, numerical implementation and examples. *Computers and Geotechnics*, *92*, 132-155. https://doi.org/10.1016/j.compgeo.2017.07.021

This material is protected by copyright and other intellectual property rights, and duplication or sale of all or part of any of the repository collections is not permitted, except that material may be duplicated by you for your research use or educational purposes in electronic or print form. You must obtain permission for any other use. Electronic or print copies may not be offered, whether for sale or otherwise to anyone who is not an authorised user.

Computers and Geotechnics 92 (2017) 132–155

Contents lists available at ScienceDirect

Computers and Geotechnics

journal homepage: www.elsevier.com/locate/compgeo

Research Paper

A study on how to couple thermo-hydro-mechanical behaviour of unsaturated soils: Physical equations, numerical implementation and examples

Ayman A. Abed *, Wojciech T. Sołowski

Aalto University, Department of Civil Engineering, P.O. Box 12100, FI-00076 Aalto, Finland

ARTICLE INFO

Article history:
Received 30 December 2016
Received in revised form 29 June 2017
Accepted 26 July 2017

Keywords:
Finite element method
Multiphase flow
Bentonite
THM behaviour
Nuclear waste repositories

ABSTRACT

This paper describes a thermo-hydro-mechanical framework suitable for modelling the behaviour of unsaturated soils. In particular, this paper focuses on bentonite clay subjected to a thermo-hydro-mechanical load, as in the case of nuclear waste engineering barriers. The paper gives a theoretical derivation of the full set of coupled balance equations governing the material behaviour as well as an extended physical interpretation. Finally, a finite element discretisation of the equations and number of simulations verifying their implementation into a custom finite element code is provided. Some aspects of the formulation are also validated against experimental data.

© 2017 Elsevier Ltd. All rights reserved.

1. Introduction

In some engineering applications the understanding of unsaturated soil behaviour becomes inevitably important and necessary for an effective design. A pronounced example is the case of bentonite which is the material of choice for engineering barriers due to its very low permeability, relative resistance to chemicals and swelling behaviour upon wetting. For instance, bentonite is used as barriers for nuclear waste disposal sites where safety specifications are especially strict [1,2]. Ideally, barriers should be nearly impermeable, self-healing (so the influence of cracks and initial imperfections is minimised) and possess properties such that the surrounding environment remains unaffected by radioactive waste materials for a very long time, typically tens of thousands of years. A suitable barrier material design requires prediction of complex behaviour under high temperature gradient, hydraulic processes and development of gas pressure. The design also requires prediction of the self-healing properties obtained due to swelling upon wetting and high pressure state in the material. Nonetheless, the developed swelling pressure should not be too high, as that could adversely affect the containers for the nuclear material. Finally, the material is also affected by radioactivity and chemical reactions, though these factors are not included in this study.

A significant body of research accumulated for these sealing materials (e.g. [3,4]), which generally agree that the modelling should consider the fully coupled (chemo)-thermo-hydro-mechanical behaviour of bentonite. This paper presents a physical framework which can be extended to include chemical effects and radioactivity effects. The framework is general and suitable for unsaturated soils and geomaterials. It can also be used for porous materials, as each constitutive equation can be easily replaced by another formulation more suitable for given application.

Experience gained in different scientific disciplines [3,5–8] suggests that the finite element method is one of the best methods to numerically solve such a coupled system of equations. This study presents in details the coupled physical formulation, finite element discretisation and implementation of the thermo-hydro-mechanical equations governing the behaviour of porous geomaterials. This paper also discusses Barcelona Basic Model (BBM) [9] and its thermo-mechanical extension [10].

Finally, this paper provides verification and validation against analytical solutions, well-established THM code (CODE_BRIGHT [11]) results, and experimental data. The numerical results are satisfactory from the point of view of matching theoretical solutions and approaching real physical behaviour.

Despite focusing on bentonite behaviour, the described physical framework is general and may be used for simulation of THM

* Corresponding author.
E-mail address: ayman.abed@aalto.fi (A.A. Abed).

http://dx.doi.org/10.1016/j.compgeo.2017.07.021
0266-352X/© 2017 Elsevier Ltd. All rights reserved.

Nomenclature

Roman

A	auxiliary term
A_o	amplitude, Θ
$\boldsymbol{A}$	Jacobian matrix
B	auxiliary term
$\boldsymbol{b}$	body force vector, M L^{-2} T^{-2}
c	volumetric heat capacity, M L^{-1} T^{-2} Θ^{-1}
c_k^i	specific heat capacity of component k in phase i, L^2 T^{-2} Θ^{-1}
C	auxiliary term
D	auxiliary term
D_{atm}	molecular diffusivity of water vapour in air, L^2 T^{-1}
$\boldsymbol{D}^e$	elastic stiffness matrix
D_{vT}	molecular diffusivity due to temperature, M L^{-1} T^{-1} Θ^{-1}
D_{vw}	molecular diffusivity due to moisture, M L^{-2} T^{-1}
E	Young's modulus, M L^{-1} T^{-2}
E_{Tk}^i	thermodynamic state function of component k in phase i
e	Euler's number or Napier's constant
F	yield function
f_{Tv}	thermal enhancement factor
$\boldsymbol{f}_u$	external forces vector, M L^{-1} T^{-2}
G	shear modulus, M L^{-1} T^{-2}
g	earth gravity acceleration, L T^{-2}
g_α, g_n, g_m	van Genuchten curve fitting parameters
H	Henry's volumetric coefficient of solubility
H_c	Henry's constant, M L^{-1} T^{-2}
h_g	gas pressure head, L
$\widehat{\boldsymbol{h}}_g$	nodal gas pressure head, L
h_w	water pressure head, L
$\widehat{\boldsymbol{h}}_w$	Nodal water pressure head, L
$\boldsymbol{j}_k^i$	non-advective flux of component k, M L^{-2} T^{-1}
K	material bulk modulus, M L^{-1} T^{-2}
k	BBM parameter
K^g	gas phase hydraulic conductivity, L T^{-1}
K_{dry}^g	gas phase dry hydraulic conductivity, L T^{-1}
k_{dry}^g	gas phase dry intrinsic permeability, L^{-2}
K^l	liquid phase hydraulic conductivity, L T^{-1}
K_{sat}^l	liquid phase saturated hydraulic conductivity, L T^{-1}
k_{ref}^l	liquid phase reference permeability, L^{-2}
k_{sat}^l	liquid phase saturated intrinsic permeability, L^{-2}
l	length, L
L	latent heat of water vaporization, L^2 T^{-2}
$\boldsymbol{M}_{ij}, \boldsymbol{K}_{ij}, \boldsymbol{f}_i$	terms being defined in Appendix B
$\boldsymbol{M}$	material stiffness matrix
M	slope of critical state line
M_a	molar mass of dry air, M mol^{-1}
M_w	molar mass of vapour, M mol^{-1}
$\boldsymbol{m}$	auxiliary vector, {1, 1, 1, 0, 0, 0}
$\boldsymbol{N}_a$	basis function
$\boldsymbol{N}_b$	shape function
$\boldsymbol{n}$	normal vector
n	porosity
n_{ref}	reference porosity
P_{atm}	atmospheric pressure, M L^{-1} T^{-2}
P_g	total gas pressure, M L^{-1} T^{-2}
P_l	liquid pressure, M L^{-1} T^{-2}
P_v	vapour partial pressure, M L^{-1} T^{-2}
p_o	isotropic preconsolidation pressure, M L^{-1} T^{-2}
p	mean net pressure, M L^{-1} T^{-2}
p_{ref}^o	reference mean pressure, M L^{-1} T^{-2}
p_o^*	saturated isotropic preconsolidation pressure at reference temperature, M L^{-1} T^{-2}
p_{oi}^*	saturated isotropic preconsolidation at the beginning of loading step i, M L^{-1} T^{-2}
p_{oT}^*	saturated isotropic preconsolidation pressure at temperature T, M L^{-1} T^{-2}
p^c	reference pressure in BBM
p_w	water pressure, M L^{-1} T^{-2}
p_{wo}	reference water pressure, M L^{-1} T^{-2}
Q	plastic potential function
Q_k^i	sink/source term of component k, M L^{-3} T^{-1}
$\boldsymbol{q}$	Darcy velocity, L T^{-1}
$\widehat{\boldsymbol{q}}$	boundary flux vector
q	deviatoric stress, M L^{-1} T^{-2}
$\boldsymbol{q}_h$	total heat flux, M T^{-3}
q_{inf}	infiltration rate, L T^{-1}
$\boldsymbol{q}^T$	conductive heat flux, M T^{-3}
$\boldsymbol{R}$	residuals matrix
R	universal gas constant, M L^2 T^{-2} Θ^{-1}mol^{-1}
RH	relative humidity
r	BBM parameter
S	degree of saturation
S_{dry}^g	gas degree of saturation at completely dry system
S_{res}^g	gas degree of saturation at the residual state
S_{abs}^l	absorbed portion of degree of saturation
S_{res}^l	degree of saturation at the residual state
S_{sat}^l	degree of saturation at full saturation
s	suction, M L^{-1} T^{-2}
T	absolute temperature, Θ
T_o	reference absolute temperature, Θ
T_{ref}	temperature equals to 273.16 K, Θ
$\widehat{\boldsymbol{T}}$	Nodal temperature, Θ
$\overline{T}$	average temperature, Θ
$\boldsymbol{t}$	boundary traction vector, M L^{-2} T^{-2}
t	time, T
tr()	trace operator
$\widehat{\boldsymbol{u}}$	Nodal displacements, L
$\boldsymbol{u}$	solid matrix displacement vector, L
v	specific volume
$\boldsymbol{v}^i$	velocity of phase i, L T^{-1}
v_v	Mass flow factor
$\boldsymbol{X}$	storage for system unknowns
z	vertical position, L

Greek

α	BBM non-associate plasticity coefficient
α_o, α_2	elastic thermal strain parameters
α_1, α_3	parameters control thermal effects on preconsolidation pressure
α_κ	parameter controls κ value
$\alpha_{\kappa s1}, \alpha_{\kappa s2}$	parameters control κ_s value
α_{swell}	material hydraulic parameter
β_{sp}	coefficient of solid particles compressibility, M^{-1} L T^2
β_{sT}	coefficient of volumetric thermal expansion of solid particles, Θ^{-1}
β_{wp}	coefficient of water compressibility, M^{-1} L T^2
β_{wT}	coefficient of volumetric thermal expansion of water, Θ^{-1}
β	BBM parameter, M^{-1} L T^2
Δ	increment
$\boldsymbol{\varepsilon}$	strain vector
$\dot{\boldsymbol{\varepsilon}}_e$	total elastic strain rate vector
$\dot{\varepsilon}_e^s$	elastic strain rate due to suction
$\dot{\boldsymbol{\varepsilon}}_e^\sigma$	elastic strain rate due to net stress vector
$\dot{\varepsilon}_e^T$	elastic strain rate due to temperature
$\dot{\boldsymbol{\varepsilon}}_p$	plastic strain rate vector

$\dot{\varepsilon}_p^v$	plastic volumetric strain rate
ε_v	infinitesimal volumetric strain
δ	increment
γ_T	material constant
Φ_h	soil heat capacity, M L^{-1} T^{-2}
ϕ^i	volume fraction of phase i
Γ	boundary of the domain Ω
κ	isotropic swelling index
κ_o	reference isotropic swelling index
κ_s	swelling index due to suction
κ_{so}	reference swelling index due to suction
Λ	plastic multiplier
λ	isotropic compression index at full saturation
λ_{dry}	thermal conductivity of dry material, M L T^{-3} Θ^{-1}
λ_s	isotropic compression index at a constant suction
λ_{sat}	thermal conductivity saturated material, M L T^{-3} Θ^{-1}
λ_T	thermal conductivity, M L T^{-3} Θ^{-1}
ν	Poisson's ratio
μ_g	gas phase dynamic viscosity, M L^{-1} T^{-1}
μ_l	liquid phase dynamic viscosity, M L^{-1} T^{-1}
ρ_a	dry air density, M L^{-3}
ρ^b	bulk density, M L^{-3}
ρ^i	density of phase i, M L^{-3}
ρ_k^i	density of component k in phase i, M L^{-3}
ρ_w^g	water vapour density, M L^{-3}
ρ_{wo}^g	saturated water vapour density, M L^{-3}
ρ_{wo}^l	reference water density, M L^{-3}
ρ^s	solid particles density, M L^{-3}
ρ^{so}	reference solid particles density, M L^{-3}
ρ^T	thermal BBM parameter
$\boldsymbol{\sigma}$	net stress vector, M L^{-1} T^{-2}
σ^t	surface tension of water, M T^{-2}
σ_o^t	reference surface tension, M T^{-2}
$\boldsymbol{\sigma}^{tot}$	total stress tensor, M L^{-1} T^{-2}
τ	tortuosity
ω	radial frequency, T^{-1}
ω_k^i	mass fraction of component k in phase i
ξ_n^T	curve fitting parameter, Θ^{-1}
ξ_w^T	curve fitting parameter, Θ^{-1}
ψ	matric suction head, L
Ω	domain
$\dot{\cdot}$	derivation with respect to time
∂	partial differentiation operator
$\boldsymbol{\nabla}$	gradient operator
$\boldsymbol{\nabla}\cdot$	divergence operator

Superscripts

e	elastic
g	gas phase
i	phase ($i = l, g, s$)
j	iteration level
l	liquid phase
m	component summation indicator
s	solid phase
tot	total
v	volumetric
ξ	relative permeability curve fitting parameters, L^{-1}

Subscripts

a	dry air component
e	elastic
g	gas phase
k	component ($k = a, w, s$)
p	plastic
s	solids component
T	temperature
u	refers to mechanical effect
v	water vapour
w	water component

Abbreviations

1D	one dimensional
BBM	Barcelona basic model
FE	finite element
THM	thermo-hydro-mechanical

coupled behaviour of a variety of geomaterials. Therefore, in what follows the terms bentonite, soil, or geomaterial are used interchangeably. The scope of application of the code can be easily extended to include other fields such as geothermal energy extraction [12,13] or freezing and thawing behaviour of soils [14,15]. The framework is also suitable for saturated and unsaturated soils due to the fact that unnecessary physical couplings can be easily removed.

The presented physical framework is complete from the point of view of taking into account thermal, hydraulic and mechanical effects in unsaturated material. The framework does not only gather different components which were not necessarily used together beforehand, but also contains a number of extensions which were previously omitted or disregarded. Those include: (1) more accurate dry air and thermal energy balance equations; (2) a derivation of an explicit formula for the plastic multiplier in case of thermo-mechanical BBM; (3) new implementation of the effect of temperature on the water retention curve with its consequences on the governing balance equations and (4) a full presentation of the finite element discretisation of the balance equations. In the latter point lies the main significance of this contribution as it also compiles a number of physical equations in a single paper, creating a useful reference. In addition, the paper shows verification and validation of the finite element method implementation, giving unique solutions to benchmark problems.

2. Governing equations

This section gathers all the constitutive models, physical assumptions and mathematical equations used in the framework. These include mass and energy balance and associated constitutive equations.

2.1. Mass balance equations

The framework uses an assumption that a porous geomaterial is continuous with three phases: liquid (l), gas (g) and solid (s) each sharing a unified point of the studied domain. The gas phase consists of dry air and water vapour, the liquid phase consists of liquid water and dissolved dry air, and the solid phase is composed of soil grains, see Fig. 1(a) and (b). It is assumed that the solid phase does not dissolve or sublimate, and as such is only subjected to thermal and mechanical effects (Section 2.1.1). However, liquid water may evaporate and water vapour may condensate (Section 2.1.2). Similarly, it is taken into account that air is soluble in water (Section 2.1.3).

This idealization separates the geomaterial into three distinct components: (1) water (w) being in liquid and vapour states; (2) dry air (a) being distributed in the voids and dissolved in the liquid phase and (3) solids (s), see Fig. 1(c). For a reference unit volume, the gas and liquid phases together occupy voids represented by

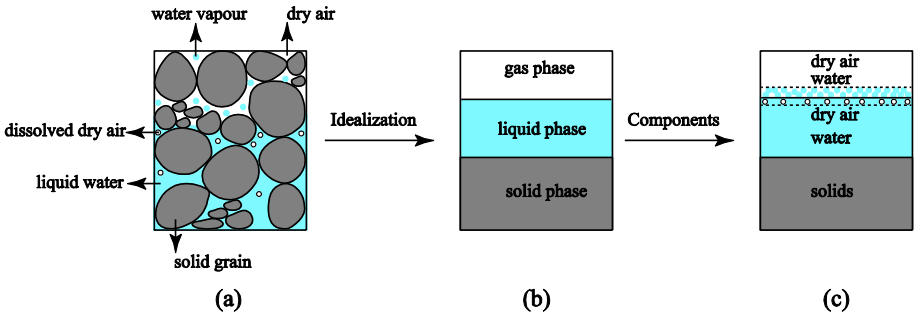

Fig. 1. Phases and components in unsaturated soil.

the soil porosity n whereas the solid phase occupies the remaining volume fraction $\phi^s = (1-n)$. The liquid degree of saturation S^l measures the void volume fraction occupied by the liquid phase $\phi^l = nS^l$ whereas the gas degree of saturation S^g measures the void volume fraction occupied by the gas phase $\phi^g = nS^g$ with constraint $S^l + S^g = 1$. This paper adopts the compositional approach of [16,17] for developing the balance equations, while the mass conservation is considered for each component instead of each phase. As a consequence, the mass balance during phase transition is implicitly taken into account without the need for special treatment.

The general mass balance equation for the component k in phase i is expressed as [7,16,18]:

$$\underbrace{\frac{\partial\left(\phi^i\rho^i\omega_k^i\right)}{\partial t}}_{storage} + \underbrace{\nabla\cdot\left(\phi^i\rho^i\omega_k^i\boldsymbol{v}^i\right)}_{advection} + \underbrace{\nabla\cdot\boldsymbol{j}_k^i}_{non-advection} = \underbrace{Q_k^i}_{sink/source} \tag{1}$$

where the symbols ϕ^i and ρ^i denote volume fraction and density of the phase i ($i = s, l, g$). The mass fraction of component k in the i-phase is expressed by $\omega_k^i = \rho_k^i/\rho^i$. The phase-velocity vector is represented by $\boldsymbol{v}^i$ whereas $\boldsymbol{j}_k^i$ is the non-advective flux vector of the component k. The gradient is denoted by ∇ and the inner product is denoted by the dot. The combined symbol " $\nabla\cdot$ " is the divergence operator.

Eq. (1) describes mass transport carried out by advection (normal fluid flow) and non-advective mechanisms (e.g., diffusion or dispersion). Additionally, the soil can store or lose fluid mass over time (e.g., due to mechanical deformations). It also shows through the term Q_k^i that a component may gain or lose mass directly by the existence of sources or sinks in the studied domain, e.g., due to chemical reactions.

For a reference unit volume, the sum of volume fractions over the three phases equals unity, that is, $\sum_i^3 \phi^i = 1$. Furthermore, the sum of the mass fraction over m components in a certain phase equals one, i.e., $\sum_k^m \omega_k^i = 1$, where $m = 2$ for gas and liquid phase and $m = 1$ for solid phase. In order to ensure mass balance, the sum of the non-advective terms within one phase vanishes such that $\sum_k^m \boldsymbol{j}_k^i = 0$ and in the absence of any external sink or source in the domain, the sum $\sum_i^3 Q_k^i$ for the component k over all three phases also vanishes. The equation of mass conservation for one phase may be constructed by the summation of the equations of each component in the corresponding phase. As a consequence of Eq. (1) and the aforementioned discussion, the mass balance equation for the i-phase becomes:

$$\frac{\partial\left(\phi^i\rho^i\right)}{\partial t} + \nabla\cdot\left(\phi^i\rho^i\boldsymbol{v}^i\right) = 0 \tag{2}$$

2.1.1. Mass balance of solid component

Similarly to the derivation of Eq. (2), the mass balance equation for solid component is:

$$\frac{\partial(\phi^s\rho^s)}{\partial t} + \nabla\cdot(\phi^s\rho^s\boldsymbol{v}^s) = 0, \tag{3}$$

where the solid particle density ρ^s is commonly taken as a function of the mean net pressure p and the absolute temperature T [18]:

$$\rho^s = \rho^{so} e^{\beta_{sp}\left(p - p_{ref}^o\right) - \beta_{sT}(T - T_o)}, \tag{4}$$

where ρ^{so} is a reference solid particle density at a reference mean net pressure p_{ref}^o and a reference absolute temperature T_o. The solid particle compressibility is taken into account through the coefficient β_{sp}, while the soil density variation with temperature is controlled by the volumetric thermal expansion coefficient β_{sT}. In general, the solid density increases with pressure and decreases with increasing temperature. The evolution of solid density in time can be described using the chain rule,

$$\frac{\partial\rho^s}{\partial t} = \frac{\partial\rho^s}{\partial p}\frac{\partial p}{\partial t} + \frac{\partial\rho^s}{\partial T}\frac{\partial T}{\partial t} = \beta_{sp}\rho^s\frac{\partial p}{\partial t} - \beta_{sT}\rho^s\frac{\partial T}{\partial t} \tag{5}$$

On expanding the time derivative and divergence operator in Eq. (3) and noting that $\phi^s = (1-n)$,

$$(1-n)\frac{\partial\rho^s}{\partial t} - \rho^s\frac{\partial n}{\partial t} + (1-n)\rho^s\nabla\cdot\boldsymbol{v}^s + (1-n)\boldsymbol{v}^s\cdot\nabla\rho^s + \rho^s\boldsymbol{v}^s\cdot\nabla(1-n) = 0 \tag{6}$$

Assuming slow deformation velocity of the solid matrix, that is $\boldsymbol{v}^s \approx 0$ and employing Eq. (5), porosity variation over time reads:

$$\frac{\partial n}{\partial t} = (1-n)\left(\nabla\cdot\boldsymbol{v}^s + \beta_{sp}\frac{\partial p}{\partial t} - \beta_{sT}\frac{\partial T}{\partial t}\right) \tag{7}$$

Furthermore, by employing the definitions of solid matrix velocity $\boldsymbol{v}^s$ and the infinitesimal volumetric strain ε_v, the divergence of solid matrix velocity $\nabla\cdot\boldsymbol{v}^s$ can be linked to the rate of volumetric strains as follows:

$$\boldsymbol{v}^s = \frac{\partial\boldsymbol{u}}{\partial t};\quad \varepsilon_v = \nabla\cdot\boldsymbol{u} \overset{\text{yields}}{\rightarrow} \nabla\cdot\boldsymbol{v}^s = \nabla\cdot\left(\frac{\partial\boldsymbol{u}}{\partial t}\right) = \frac{\partial(\nabla\cdot\boldsymbol{u})}{\partial t} = \frac{\partial\varepsilon_v}{\partial t} \tag{8}$$

where $\boldsymbol{u}$ is the solid matrix displacements vector. Hence, the evolution of soil porosity in time is:

$$\frac{\partial n}{\partial t} = (1-n)\left(\frac{\partial\varepsilon_v}{\partial t} + \beta_{sp}\frac{\partial p}{\partial t} - \beta_{sT}\frac{\partial T}{\partial t}\right) \tag{9}$$

This expression implies that soil porosity is affected by variations in soil temperature, mechanical pressure on solid grains, and mechanical deformations of the soil matrix. This is especially important, as this is the main source of mechanical coupling in the governing balance equations. However, due to the negligible

effect of the compressibility of soil solid grains in comparison to the contributions of other terms in Eq. (9), the simplification $\beta_{sp} = 0$ is adopted subsequently.

2.1.2. Mass balance of water component

Writing the mass balance equation (1) for the water component ($k = w$) in the three phases $i = l, g, s$ yields the following global water mass balance equation:

$$\underbrace{\frac{\partial\left(\phi^l \rho^l \omega_w^l\right)}{\partial t} + \nabla\cdot\left(\phi^l \rho^l \omega_w^l \boldsymbol{v}^l\right) + \nabla\cdot\boldsymbol{j}_w^l}_{\text{water in liquid phase}} + \underbrace{\frac{\partial(\phi^g \rho^g \omega_w^g)}{\partial t} + \nabla\cdot\left(\phi^g \rho^g \omega_w^g \boldsymbol{v}^g\right) + \nabla\cdot\boldsymbol{j}_w^g}_{\text{water in gas phase}} + \underbrace{0}_{\text{water in solid phase}} = 0 \tag{10}$$

where

$$\phi^l \rho^l \omega_w^l = n S^l \rho^l \left(\frac{\rho_w^l}{\rho^l}\right) = n S^l \rho_w^l \tag{11}$$

represents the water component mass in the liquid phase and

$$\phi^g \rho^g \omega_w^g = n S^g \rho^g \left(\frac{\rho_w^g}{\rho^g}\right) = n\left(1 - S^l\right)\rho_w^g \tag{12}$$

represents the water component mass in the gas phase. The liquid phase velocity vector $\boldsymbol{v}^l$ and the gas phase velocity vector $\boldsymbol{v}^g$ are given as the sum of the solid phase velocity $\boldsymbol{v}^s$ and the average fluid phase velocity [19]:

$$\boldsymbol{v}^l = \frac{\boldsymbol{q}^l}{nS^l} + \boldsymbol{v}^s, \quad \boldsymbol{v}^g = \frac{\boldsymbol{q}^g}{nS^g} + \boldsymbol{v}^s, \tag{13}$$

where $\boldsymbol{q}$ is the specific discharge (Darcy velocity) of the fluid phase.

As the liquid phase includes liquid water with a small amount of dissolved dry air, the non-advective mass transfer mechanisms are negligible within this phase i.e. $\nabla\cdot\boldsymbol{j}_w^l = 0$. In other words, that means that we neglect any movement of water in the liquid phase due to differences in dissolved air concentration. Employing formulas (11)–(13), Eq. (10) can be rewritten as:

$$\frac{\partial\left(nS^l\rho_w^l\right)}{\partial t} + \frac{\partial(nS^g\rho_w^g)}{\partial t} + \nabla\cdot\left(nS^l\rho_w^l\boldsymbol{v}^l\right) + \nabla\cdot\left(nS^g\rho_w^g\boldsymbol{v}^g\right) + \nabla\cdot\boldsymbol{j}_w^g = 0 \tag{14}$$

On expanding Eq. (14) and taking into account the assumption of a slowly deforming soil with $\boldsymbol{v}^s \approx 0$, this becomes:

$$\begin{aligned} &-(1-n)\left(S^l\rho_w^l + S^g\rho_w^g\right)\beta_{sT}\frac{\partial T}{\partial t} + \left(S^l\rho_w^l + S^g\rho_w^g\right)\frac{\partial\varepsilon_v}{\partial t} \\ &+ n\left(\rho_w^l - \rho_w^g\right)\frac{\partial S^l}{\partial t} + nS^l\frac{\partial\rho_w^l}{\partial t} + nS^g\frac{\partial\rho_w^g}{\partial t} + \nabla\cdot\left(\rho_w^l\boldsymbol{q}^l\right) \\ &+ \nabla\cdot\left(\rho_w^g\boldsymbol{q}^g\right) + \nabla\cdot\boldsymbol{j}_w^g = 0 \end{aligned} \tag{15}$$

The terms of this equation are discussed separately in the following subsections.

2.1.2.1. Liquid water density. Similarly to the solid particle density, the liquid water density ρ_w^l depends on the pore-water pressure p_w and the temperature T according to the formula [18]

$$\rho_w^l = \rho_{wo}^l e^{\beta_{wp}(p_w - p_{wo}) - \beta_{wT}(T - T_o)} \tag{16}$$

where ρ_{wo}^l is the reference water density at reference pore-water pressure p_{wo}, and T_o is a reference temperature. The symbols β_{wp} and β_{wT} denote the water compressibility coefficient and the water volumetric thermal expansion coefficient, respectively. It follows from Eq. (16) that the liquid water density varies over time according to

$$\frac{\partial\rho_w^l}{\partial t} = \frac{\partial\rho_w^l}{\partial T}\frac{\partial T}{\partial t} + \frac{\partial\rho_w^l}{\partial p_w}\frac{\partial p_w}{\partial h_w}\frac{\partial h_w}{\partial t} = -\beta_{wT}\rho_w^l\frac{\partial T}{\partial t} + \beta_{wp}g\rho_w^{l^2}\frac{\partial h_w}{\partial t}, \tag{17}$$

where g denotes the earth gravity acceleration.

2.1.2.2. Degree of saturation and hydraulic conductivity. In the case of a partially saturated soil, the water degree of saturation depends on suction and other factors including temperature and soil dry density [20,21]. For the scope of this paper, only the influence of suction and temperature on the degree of saturation is considered, i.e. S^l is a function of ψ and T only. The matric suction head ψ is defined as the difference between the gas pressure head h_g and the pore-water pressure head h_w,

$$\psi = h_g - h_w \tag{18}$$

If variations of suction head and temperature are known over time, the variation of the degree of saturation in time is given by

$$\begin{aligned} \frac{\partial S^l}{\partial t} &= \frac{\partial S^l}{\partial\psi}\frac{\partial\psi}{\partial h_g}\frac{\partial h_g}{\partial t} + \frac{\partial S^l}{\partial\psi}\frac{\partial\psi}{\partial h_w}\frac{\partial h_w}{\partial t} + \frac{\partial S^l}{\partial T}\frac{\partial T}{\partial t} \\ &= \frac{\partial S^l}{\partial\psi}\left(\frac{\partial h_g}{\partial t} - \frac{\partial h_w}{\partial t}\right) + \frac{\partial S^l}{\partial T}\frac{\partial T}{\partial t} \end{aligned} \tag{19}$$

Hence a constitutive assumption connecting the soil saturation to suction head and temperature is necessary in order to evaluate the derivatives in Eq. (19). Although many expressions are available in the literature [22], the van Genuchten [23] model is used in this study:

$$S^l = \left(S_{sat}^l - S_{res}^l\right)\left[1 + (g_\alpha|\psi|)^{g_n}\right]^{g_m} + S_{res}^l \tag{20}$$

The symbols S_{res}^l and S_{sat}^l stand for degree of saturation at the residual state and at full saturation, respectively. Usually $S_{sat}^l = 1.0$ and S_{res}^l is considered as a fitting parameter in the absence of any laboratory measurements. The formula has three fitting parameters: g_α, g_n and g_m, all of which are temperature dependent as proposed in [20]. To find the parameters, a linear relationship is assumed between surface tension of water σ^t and the absolute temperature T [20]:

$$\sigma^t = 0.118 - 1.54\times10^{-4}T \tag{21}$$

Eq. (21) yields a value of $\sigma_o^t = 0.07285$ N/m for the surface tension of water at the reference absolute temperature T_o = 293.16 K (20 °C). The fitting parameters of van Genuchten model g_α, g_n and g_m at temperature T relate to the reference values $g_{\alpha o}$, g_{no} measured at the reference temperature T_o as follows,

$$g_\alpha = (\sigma_o^t/\sigma^t)g_{\alpha o}; \quad g_n = \frac{g_{no}}{1 - \xi_n^T g_{no}(T - T_o)}; \quad g_m = \frac{1}{g_n} - 1 \tag{22}$$

Furthermore, the degree of saturation at zero suction S_{so}^l is considered temperature dependent according to the following formula:

$$S_{so}^l = S_{sat}^l + \xi_w^T(T - T_o) \tag{23}$$

In the above formulas ξ_n^T and ξ_w^T are material parameters to be determined experimentally. They describe the sensitivity of the soil water characteristic curve to the temperature variations. Upon considering the temperature effect on van Genuchten parameters in Eq. (20), the variation in degree of saturation with temperature variation can be evaluated,

$$\frac{\partial S^l}{\partial T} = \frac{\partial S^l}{\partial S_{so}^l}\frac{\partial S_{so}^l}{\partial T} + \frac{\partial S^l}{\partial g_\alpha}\frac{\partial g_\alpha}{\partial T} + \frac{\partial S^l}{\partial g_n}\frac{\partial g_n}{\partial T}, \tag{24}$$

where the terms of Eq. (24) are derived and given in Appendix A.

The hydraulic conductivity coefficient K^l (see Section 2.1.2.4), is also a function of temperature and saturation. Great many empirical expressions can describe this relationship [24]. However, [25–27] suggest that the following formula provides an acceptable fitting of the physical measurements for bentonite:

$$K^l = K^l_{sat}\left(\frac{S^l - S^l_{res}}{S^l_{sat} - S^l_{res}}\right)^3 \tag{25}$$

where K^l_{sat} is the hydraulic conductivity at full saturation in terms of saturated intrinsic permeability k^l_{sat} as follows:

$$K^l_{sat} = \frac{g\rho^l_w k^l_{sat}}{\mu_l} \tag{26}$$

where μ_l is the liquid dynamic viscosity. In case of water, the viscosity is considered to be temperature dependent according to the following empirical formula [28]:

$$\mu_l = \left(243.18 \times 10^{-7}\right)10^{\frac{247.8}{T-140}} \tag{27}$$

The dependency of saturated intrinsic permeability on soil porosity is introduced using the Carmen-Kozeny relation [29,30]:

$$k^l_{sat} = k^l_{ref}\frac{n^3}{(1-n)^2}\frac{(1-n_{ref})^2}{n^3_{ref}} \tag{28}$$

where k^l_{ref} is a reference saturated intrinsic permeability at a reference porosity n_{ref}. Similar hydraulic conductivity function to that in Eq. (20) may be used for gas [11]:

$$K^g = K^g_{dry}\left(\frac{S^g - S^g_{res}}{S^g_{dry} - S^g_{res}}\right)^3, \tag{29}$$

where K^g_{dry} is the gas hydraulic conductivity at completely dry state. The symbols S^g_{dry} and S^g_{res} stand for gas degree of saturation of a fully dry system and at the residual state (near full water saturation), respectively. Usually $S^g_{dry} = 1.0$ and S^g_{res} is considered as a fitting parameter in the absence of any laboratory measurements. The gas hydraulic conductivity for fully dry system K^g_{dry} is given in terms of intrinsic gas permeability k^g_{dry},

$$K^g_{dry} = \frac{g\rho^l_w k^g_{dry}}{\mu_g} \tag{30}$$

The gas viscosity μ_g is assumed to be temperature dependent according to the following formula [31]:

$$\mu_g = 1.48 \times 10^{-6}\frac{\sqrt{T}}{1+\frac{119}{T}} \tag{31}$$

The above equation estimates the gas viscosity in [kg/m/s].

2.1.2.3. Water vapour density. The density of water vapour in the gas phase ρ^g_w is taken as [7]

$$\rho^g_w = RH\rho^g_{wo}, \tag{32}$$

where RH is the relative humidity

$$RH = e^{\frac{-gM_w\psi}{RT}} \tag{33}$$

and ρ^g_{wo} $[\mathrm{kg/m^3}]$ is the empirically estimated saturated water vapour density, a function of temperature [32]

$$\rho^g_{wo} = 10^{-3}e^{19.891-\frac{4974.0}{T}} \tag{34}$$

In the above equations T is estimated in Kelvin, $R = 8.3144$ J/mol/K is the universal gas constant and $M_w = 0.018016$ kg/mol is the molar mass of vapour. Other equally valid empirical formulas are available in literature [4], all of these correlations provide excellent fit to the experimental data. Employing Eqs. (33), (34) in (32) yields the following formula for the variation of water vapour density over time:

$$\begin{aligned}\frac{\partial\rho^g_w}{\partial t} &= \frac{\partial\rho^g_w}{\partial T}\frac{\partial T}{\partial t} + \frac{\partial\rho^g_w}{\partial\psi}\frac{\partial\psi}{\partial h_w}\frac{\partial h_w}{\partial t} + \frac{\partial\rho^g_w}{\partial\psi}\frac{\partial\psi}{\partial h_g}\frac{\partial h_g}{\partial t}\\ &= \left[\frac{\rho^g_w}{T^2}\left(4974.0 + \frac{gM_w\psi}{R}\right)\right]\frac{\partial T}{\partial t} + \frac{\rho^g_w gM_w}{RT}\left(\frac{\partial h_w}{\partial t} - \frac{\partial h_g}{\partial t}\right),\end{aligned} \tag{35}$$

showing that the vapour density is affected by the temperature and suction variations in the soil.

2.1.2.4. Advective liquid and gas flow. The advective fluid flux obeys Darcy's phenomenological law, where the fluid mass flows proportionally to the fluid total potential gradient. For liquid phase, the flux is:

$$\boldsymbol{q}^l = -K_l(\nabla h_w + 1), \tag{36}$$

and the advective gas flux is given as:

$$\boldsymbol{q}^g = -K_g\left(\nabla h_g + \frac{\rho^g}{\rho^l_w}\right), \tag{37}$$

where h_g is the gas pressure head being equal to the equivalent water pressure head. The gas pressure at any time is calculated as $P_g = \rho^l_w g h_g$. For an ideal gas, the total gas pressure P_g is the sum of the partial pressures of its components:

$$P_g = P_v + P_a, \tag{38}$$

where P_v and P_a are the partial pressure of water vapour and dry air respectively. The density of dry air ρ^g_a is

$$\rho^g_a = \frac{M_a P_a}{RT}, \tag{39}$$

with molar mass of dry air $M_a = 0.0288$ kg/mol. The partial vapour pressure is calculated as:

$$P_v = \frac{\rho^g_w RT}{M_w}, \tag{40}$$

Using Eqs. (38)–(40), the dry air density is therefore

$$\begin{aligned}\rho^g_a &= \frac{M_a(P_g - P_v)}{RT} = \frac{M_a\rho^l_w g h_g}{RT} - \frac{M_a\left(\frac{\rho^g_w RT}{M_w}\right)}{RT}\\ &= \frac{M_a\rho^l_w g h_g}{RT} - \frac{M_a\rho^g_w}{M_w}\end{aligned} \tag{41}$$

Finally, the total gas density ρ^g can be determined as the sum of the densities of water vapour and dry air:

$$\rho^g = \rho^g_w + \rho^g_a \tag{42}$$

2.1.2.5. Non-advective water flux. Following Philip and De Vries model [33], for non-isothermal conditions the temperature variation leads to noticeable variation in vapour pressure and moisture movement. According to their theory, the water mass flux in vapour state $\boldsymbol{j}^g_w$ can be attributed to moisture variation (suction gradient) in the system $\boldsymbol{j}^g_{vw}$ and temperature variation $\boldsymbol{j}^g_{vT}$,

$$\boldsymbol{j}^g_w = \boldsymbol{j}^g_{vw} + \boldsymbol{j}^g_{vT} = \underbrace{-D_{vw}\nabla h_w + D_{vw}\nabla h_g}_{\text{moisture term}} - \underbrace{D_{vT}\nabla T}_{\text{temperature term}}, \tag{43}$$

where

$$D_{vw} = D_{atm}\, v_v \phi^g \tau \rho_w^g \frac{gM_w}{RT} \tag{44}$$

and

$$D_{vT} = f_{Tv} D_{atm}\, v_v \phi^g \tau \rho_w^g \left[\frac{4974.0}{T^2} + \frac{gM_w\psi}{RT^2}\right] \tag{45}$$

The mass-flow factor v_v is taken as unity in this study and τ is the tortuosity. The volumetric air content of soil is represented by $\phi^g = nS^g$ and the thermal enhancement factor by f_{Tv}. The coefficient D_{atm} is the molecular diffusivity of water vapour in air, shown to depend on temperature and gas pressure by [33],

$$D_{atm} = 5.89 \times 10^{-6}\left(\frac{T^{2.3}}{P_g}\right), \tag{46}$$

where D_{atm} is estimated in "m^2/s", T in "K" and P_g in "pa". In a later publication, De Vries [34] argued that Eq. (46) gives high values for D_{atm} and proposed a modified version:

$$D_{atm} = 2.16 \times 10^{-5}\left(\frac{T}{T_{ref}}\right)^{1.8} \tag{47}$$

with $T_{ref} = 273.16$ K. Based on the experimental findings of [35,36], the product $v_v\ \phi^g$ in Eqs. (44) and (45) can be replaced by soil porosity n and

$$D_{atm} = 2.2 \times 10^{-5}\left(\frac{P_{atm}}{P_g}\right)\left(\frac{T}{T_o}\right)^{1.75} \tag{48}$$

where P_{atm} is the atmospheric pressure. These three formulations for estimating the vapour flow are implemented into the code. The calibration against experimental data usually dictates which formula to use.

As an alternative, Fick's law can be used to model the vapour diffusion process [37]. The advantage of Fick's law is that it requires fewer parameters. However, it does not explicitly separate the effects of temperature and moisture concentration on vapour diffusion. Therefore the model of Philip and De Vries has been implemented as it allows for physically meaningful separation of temperature and moisture concentration effects which leads to a better fit of experimental data.

2.1.2.6. Adopted mass balance equation of water component. By introducing the information in Sections 2.1.2.1–2.1.2.4 and 2.1.2.5 into Eq. (15) and rearranging terms, the mass balance equation of water component finally reads:

$$\begin{aligned}
&\left[n\left(\rho_w^l - \rho_w^g\right)\frac{\partial S^l}{\partial T} - (1-n)\left(S^l\rho_w^l + S^g\rho_w^g\right)\beta_{sT} - nS^l\beta_{wT}\rho_w^l\right.\\
&\left.+nS^g\frac{\rho_w^g}{T^2}\left(4974 + \frac{gM_w\psi}{R}\right)\right]\frac{\partial T}{\partial t}\\
&+\left[nS^l\beta_{wp}g\rho_w^{l^2} + nS^g\frac{\rho_w^g gM_w}{RT} - n\left(\rho_w^l - \rho_w^g\right)\frac{\partial S^l}{\partial \psi}\right]\frac{\partial h_w}{\partial t}\\
&+\left[n\left(\rho_w^l - \rho_w^g\right)\frac{\partial S^l}{\partial \psi} - nS^g\frac{\rho_w^g gM_w}{RT}\right]\frac{\partial h_g}{\partial t} + \left(S^l\rho_w^l + S^g\rho_w^g\right)\frac{\partial \varepsilon_v}{\partial t}\\
&+\nabla\cdot\left(\rho_w^l\boldsymbol{q}^l\right) + \nabla\cdot\left(\rho_w^g\boldsymbol{q}^g\right) + \nabla\cdot\boldsymbol{j}_w^g = 0
\end{aligned} \tag{49}$$

Therefore, soil water content is affected by temperature, pore-water pressure, pore-gas pressure, mechanical deformation of the solid matrix, and advection and diffusion processes.

2.1.3. Mass balance of dry air component

The mass balance equation for dry air is derived by the summation of Eq. (1) for the dry air component ($k = a$) over all the three phases ($i = l, g, s$),

$$\begin{aligned}
&\underbrace{\frac{\partial\left(\phi^l\rho^l\omega_a^l\right)}{\partial t} + \nabla\cdot\left(\phi^l\rho^l\omega_a^l\boldsymbol{v}^l\right) + \nabla\cdot\boldsymbol{j}_a^l}_{\text{dissolved dry air in liquid phase}}\\
&+\underbrace{\frac{\partial(\phi^g\rho^g\omega_a^g)}{\partial t} + \nabla\cdot\left(\phi^g\rho^g\omega_a^g\boldsymbol{v}^g\right) + \nabla\cdot\boldsymbol{j}_a^g}_{\text{dry air in soil voids}} + \underbrace{0}_{\text{dry air in solid phase}} = 0
\end{aligned} \tag{50}$$

where

$$\phi^g\rho^g\omega_a^g = nS^g\rho^g\omega_a^g = n\left(1 - S^l\right)\rho^g\left(\frac{\rho_a^g}{\rho^g}\right) = n\left(1 - S^l\right)\rho_a^g \tag{51}$$

represents the dry air mass in the gas phase. The volumetric mass of the dissolved dry air in liquid phase is obtained via Henry's volumetric coefficient of solubility H:

$$\phi^l\rho^l\omega_a^l = nHS^l\rho^l\omega_a^l = nHS^l\rho^l\left(\frac{\rho_a^l}{\rho^l}\right) = nHS^l\rho_a^l, \tag{52}$$

providing the mass of dry air dissolved in the liquid phase. It is assumed that no diffusion of dry air could happen in the liquid phase, and so $\boldsymbol{j}_a^l = 0$. Noticing the constraint $\sum_k^m j_k^i = 0$ allows for the derivation of the non-advective part of dry air mass flux in gas phase $\boldsymbol{j}_a^g$:

$$\boldsymbol{j}_a^g = -\boldsymbol{j}_w^g, \tag{53}$$

meaning that within one phase, the components can mix due to diffusion or other non-advective process but without gain or loss in that phase mass. The non-advective water flux in gas phase $\boldsymbol{j}_w^g$ is fully determined and discussed in details in Section 2.1.2.5. For the sake of simplicity, the density of dissolved dry air in water ρ_a^l is assumed to be equal to the density of the pore-dry air ρ_a^g [38]. Both will be indicated as ρ_a in the remainder of this paper. For a slowly deforming soil with $v^s \approx 0$ and taking into account Eq. (13), Eq. (45) takes the form

$$\begin{aligned}
&\frac{\partial(nS^g\rho_a)}{\partial t} + \frac{\partial\left(nHS^l\rho_a\right)}{\partial t} + \nabla\cdot\left(\rho_a\boldsymbol{q}^g\right) + \nabla\cdot\left(\rho_a H\boldsymbol{q}^l\right)\\
&+\rho_a\left[S^g + HS^l\right]\nabla\cdot\boldsymbol{v}^s - \nabla\cdot\boldsymbol{j}_w^g = 0
\end{aligned} \tag{54}$$

Upon expanding and re-arranging,

$$\begin{aligned}
&n\rho_a\left[S^g + HS^l\right]\beta_{sT}\frac{\partial T}{\partial t} + \frac{\rho_a\left[S^g + HS^l\right]}{1-n}\frac{\partial n}{\partial t} + n\left[S^g + HS^l\right]\frac{\partial \rho_a}{\partial t}\\
&+n\rho_a[H-1]\frac{\partial S^l}{\partial t} + n\rho_a S^l\frac{\partial H}{\partial T}\frac{\partial T}{\partial t} + \nabla\cdot\left(\rho_a\boldsymbol{q}^g\right)\\
&+\nabla\cdot\left(\rho_a H\boldsymbol{q}^l\right) - \nabla\cdot\boldsymbol{j}_w^g = 0
\end{aligned} \tag{55}$$

The most important terms in the above equation will be discussed in more details in the following sections.

2.1.3.1. Henry's volumetric coefficient of solubility. Based on the law of ideal gas, the Henry's volumetric coefficient of solubility is [39]

$$H = \frac{\rho_w^l}{H_c}\frac{RT}{M_w}, \tag{56}$$

where $H_c = 10^{10}$ pa is the Henry's constant [40]. The value of H varies over time in response to the variation in water pressure head h_w and temperature T according to the following formula:

$$\frac{\partial H}{\partial t} = \frac{\partial H}{\partial \rho_w^l}\frac{\partial \rho_w^l}{\partial p_w}\frac{\partial p_w}{\partial h_w}\frac{\partial h_w}{\partial t} + \frac{\partial H}{\partial T}\frac{\partial T}{\partial t}, \tag{57}$$

yielding

$$\frac{\partial H}{\partial t} = g\rho_w^l \beta_{wp} H \frac{\partial h_w}{\partial t} + \left(\frac{1}{T} - \beta_{wT}\right) H \frac{\partial T}{\partial t}, \tag{58}$$

showing that the ratio of dry air dissolution in liquid phase is not constant but varies over time. By considering Eq. (58), the current formulation of dry air mass balance equation and energy balance equation in Section 2.2 is more accurate compared to previous formulations which tend to assign a constant value for H.

2.1.3.2. Density of dry air. The density of dry air derived in Section 2.1.2.4 assumes that dry air behaves as an ideal gas. To investigate further the effects of the variation of dry air density over time, differentiation of Eq. (41) yields:

$$\frac{\partial \boldsymbol{\rho_a}}{\partial \boldsymbol{t}} = \frac{\partial \boldsymbol{\rho_a}}{\partial \boldsymbol{h_g}}\frac{\partial \boldsymbol{h_g}}{\partial \boldsymbol{t}} + \frac{\partial \boldsymbol{\rho_a}}{\partial \boldsymbol{\rho_w^g}}\frac{\partial \boldsymbol{\rho_w^g}}{\partial \boldsymbol{t}}, \tag{59}$$

which after mathematical manipulation gives

$$\frac{\partial \rho_a}{\partial t} = \left(\frac{M_a \rho_w^l g}{RT} + \frac{M_a}{M_w}\frac{\rho_w^g g M_w}{RT}\right)\frac{\partial h_g}{\partial t} - \frac{M_a}{M_w}\frac{\rho_w^g g M_w}{RT}\frac{\partial h_w}{\partial t} - \frac{M_a}{M_w}\frac{\rho_w^g}{T^2}\left(4974 + \frac{g M_w \psi}{R}\right)\frac{\partial T}{\partial t} \tag{60}$$

This shows that the evolution of dry air density in time is a function of the changes in gas pressure head, liquid pressure head and temperature.

2.1.3.3. Adopted dry air mass balance equation. After introducing the information in Sections 2.1.3.1 and 2.1.3.2 into Eq. (55) and rearranging the terms, the dry air component mass balance equation reads

$$\begin{aligned}
&\left[n\rho_a[H-1]\frac{\partial S^l}{\partial T} + n\rho_a S^l \frac{\partial H}{\partial T}\right.\\
&\left. -(1-n)\rho_a\left[S^g + HS^l\right]\beta_{sT} - n\left[S^g + HS^l\right]\frac{M_a}{M_w}\frac{\rho_w^g}{T^2}\left(4974 + \frac{gM_w\psi}{R}\right)\right]\frac{\partial T}{\partial t}\\
&-\left[n\left[S^g + HS^l\right]\frac{M_a}{M_w}\frac{\rho_w^g g M_w}{RT} + n\rho_a[H-1]\frac{\partial S^l}{\partial \psi} - n\rho_a S^l \frac{\partial H}{\partial h_w}\right]\frac{\partial h_w}{\partial t}\\
&+\left[n\left[S^g + HS^l\right]\left(\frac{M_a \rho_w^l g}{RT} + \frac{M_a}{M_w}\frac{\rho_w^g g M_w}{RT}\right) + n\rho_a[H-1]\frac{\partial S^l}{\partial \psi}\right]\frac{\partial h_g}{\partial t}\\
&+\rho_a\left[S^g + HS^l\right]\frac{\partial \varepsilon_v}{\partial t} + \nabla\cdot(\rho_a \boldsymbol{q}^g) + \nabla\cdot(\rho_a H \boldsymbol{q}^l) - \nabla\cdot\boldsymbol{j}_w^g = 0
\end{aligned} \tag{61}$$

2.2. Energy balance equation

The enthalpy balance equation is given as [4,7,41,42]

$$\underbrace{\frac{\partial \Phi_h}{\partial t}}_{\text{Heat storage}} + \underbrace{LQ_w^g}_{\text{latent heat of vaporization}} + \underbrace{\nabla\cdot\boldsymbol{q}_h}_{\text{heat due to conduction and convection}} = 0 \tag{62}$$

where Φ_h is the soil heat capacity, L is the latent heat of water vaporization, and $\boldsymbol{q}_h$ is the heat flux including conduction and convection. The rate of water vapour production Q_w^g can be determined depending on Eq. (1) as:

$$Q_w^g = \frac{\partial(nS^g\rho_w^g)}{\partial t} + \nabla\cdot(nS^g\rho_w^g \boldsymbol{v}^g) + \nabla\cdot\boldsymbol{j}_w^g \tag{63}$$

after substituting the terms with the corresponding formulas and doing the derivation, Eq. (63) reads:

$$Q_w^g = -(1-n)S^g\rho_w^g\beta_{sT}\frac{\partial T}{\partial t} + S^g\rho_w^g\frac{\partial \varepsilon_v}{\partial t} - n\rho_w^g\frac{\partial S^l}{\partial t} + nS^g\frac{\partial \rho_w^g}{\partial t} + \nabla\cdot(\rho_w^g \boldsymbol{q}^g) + \nabla\cdot\boldsymbol{j}_w^g \tag{64}$$

The important terms in the enthalpy balance equation are explained in more detail in the following subsections.

2.2.1. Soil heat capacity

The general form of the soil heat capacity is [28]

$$\Phi_h = \phi^i \rho^i \omega_k^i E_{Tk}^i \tag{65}$$

The thermodynamic state function E_{Tk}^{α} for internal energy of component k in phase i is given as [18]:

$$E_{Tk}^i = c_k^i\left(T_k^i - T_{ko}^i\right) \tag{66}$$

where c_k^i is the specific heat capacity of component k in phase i. It is assumed that the different components in the soil are in thermal equilibrium which yields $T_k^i = T$ and $T_{ko}^i = T_o$. By expanding Eq. (65) with the assumption that dissolved air in water has similar specific heat capacity to the dry pore-air, the soil heat capacity is expressed as:

$$\Phi_h = \left[(1-n)\rho^s c_s + n\left(HS^l + S^g\right)\rho_a c_a + nS^l\rho_w^l c_w^l + nS^g\rho_w^g c_w^g\right](T - T_o) \tag{67}$$

2.2.2. Heat flux

The total heat flux includes: (i) part coming from the direct conduction of heat by soil particles, (ii) part related to the convection of heat by liquid water flow and (iii) part due to the contribution of gas phase in the convection of heat. The total heat flux can be written as:

$$\boldsymbol{q}_h = \underbrace{\boldsymbol{q}^T}_{\text{conduction}} + \underbrace{\rho^i\omega_k^i E_{Tk}^i \boldsymbol{q}^i}_{\text{convection by liquid phase}} + \underbrace{E_{Tk}^i \boldsymbol{j}_w^i}_{\text{convection by gas phase}} \tag{68}$$

where $\boldsymbol{q}^T$ is the conductive heat flux:

$$\boldsymbol{q}^T = -\lambda_T \nabla T \tag{69}$$

The soil conductivity λ_T is assumed to be a function of the soil degree of saturation. The second and third terms in Eq. (68) account for the heat convection by the liquid water advection, as well as the air and water vapour diffusion. Finally, Eq. (68) yields an expression for the total heat flux:

$$\boldsymbol{q}_h = -\lambda_T\nabla T + \left[(\rho_a c_a + \rho_w^g c_w^g)\boldsymbol{q}^g + (\rho_w^l c_w^l + \rho_a c_a H)\boldsymbol{q}^l\right](T - T_o) + \left[c_w^g - c_a\right]\boldsymbol{j}_w^g(T - T_o) \tag{70}$$

2.2.3. Adopted energy balance equation

Assuming that each component has a constant specific heat capacity, the final form of the energy balance equation is:

$$
\begin{aligned}
&\left(A(1-n)+LS^g\rho_w^g\right)\frac{\partial \varepsilon_v}{\partial t}\\
&+\left[nS^l\rho_a c_a(T-T_o)\frac{\partial H}{\partial T}+(nC-Ln\rho_w^g)\frac{\partial S^l}{\partial T}-\left[A+B+(1-n)LS^g\rho_w^g\right]\beta_{sT}\right.\\
&+D-\left(n\left[HS^l c_a+S^g c_a\right](T-T_o)\right)\frac{M_a}{M_w}\frac{\rho_w^g}{T^2}\left(4974+\frac{gM_w\psi}{R}\right)\\
&+\left(\left[nS^g c_w^g\right](T-T_o)+LnS^g\right)\left[\frac{\rho_w^g}{T^2}\left(4974+\frac{gM_w\psi}{R}\right)\right]\\
&\left.-\left(\left[nS^l c_w^l\right](T-T_o)\right)\beta_{wT}\rho_w^l\right]\frac{\partial T}{\partial t}\\
&+\left[-(nC-Ln\rho_w^g)\frac{\partial S^l}{\partial \psi}-\left(n\left[HS^l c_a+S^g c_a\right](T-T_o)\right)\frac{M_a}{M_w}\frac{\rho_w^g g M_w}{RT}\right.\\
&+\left(\left[nS^l c_w^l\right](T-T_o)\right)\beta_{wp}g\rho_w^{l^2}+\left(\left[nS^g c_w^g\right](T-T_o)+LnS^g\right)\frac{\rho_w^g g M_w}{RT}\\
&\left.+nS^l\rho_a c_a(T-T_o)\frac{\partial H}{\partial h_w}\right]\frac{\partial h_w}{\partial t}\\
&+\left[(nC-Ln\rho_w^g)\frac{\partial S^l}{\partial \psi}+\left(n\left[HS^l c_a+S^g c_a\right](T-T_o)\right)\left(\frac{M_a\rho_w^l g}{RT}+\frac{M_a}{M_w}\frac{\rho_w^g g M_w}{RT}\right)\right.\\
&\left.-\left(\left[nS^g c_w^g\right](T-T_o)+LnS^g\right)\frac{\rho_w^g g M_w}{RT}\right]\frac{\partial h_g}{\partial t}+\nabla\cdot\boldsymbol{q_h}+L\nabla\cdot\left(\rho_w^g\boldsymbol{q}^g\right)+L\nabla\cdot\boldsymbol{j}_w^g=0
\end{aligned}
\tag{71}
$$

with

$$
\begin{aligned}
\nabla\cdot\boldsymbol{q_h} = &-\lambda_T\nabla\cdot\nabla T+\left[\left(\rho_a c_a+\rho_w^g c_w^g\right)\right](T-T_o)\nabla\cdot\boldsymbol{q}^g\\
&+\left[\left(\rho_a c_a+\rho_w^g c_w^g\right)\right]\boldsymbol{q}^g\cdot\nabla T\\
&+\left[\left(\rho_w^l c_w^l+\rho_a c_a H\right)\right](T-T_o)\nabla\cdot\boldsymbol{q}^l\\
&+\left[\left(\rho_w^l c_w^l+\rho_a c_a H\right)\boldsymbol{q}^l+\left[c_w^g-c_a\right]\boldsymbol{j}_w^g\right]\cdot\nabla T\\
&+\left[c_w^g-c_a\right](T-T_o)\nabla\cdot\boldsymbol{j}_w^g
\end{aligned}
\tag{72}
$$

and

$$
A=\left[-\rho^s c_s+HS^l\rho_a c_a+S^g\rho_a c_a+S^l\rho_w^l c_w^l+S^g\rho_w^g c_w^g\right](T-T_o)
$$

$$
B=[(1-n)\rho_s c_s](T-T_o)
$$

$$
C=\left[H\rho_a c_a-\rho_a c_a+\rho_w^l c_w^l-\rho_w^g c_w^g\right](T-T_o)
$$

$$
D=n\left[HS^l\rho_a c_a+S^g\rho_a c_a+S^l\rho_w^l c_w^l+S^g\rho_w^g c_w^g\right]+(1-n)\rho^s c_s
$$

Note that the adopted energy balance equation does not take into account e.g. plastic work in the material which is normally transferred into heat, or energy loss related to water flux. Those terms are normally negligible compared to the mentioned components.

2.3. Static balance of linear momentum

The local static mechanical balance equation is given as:

$$
\nabla\cdot\boldsymbol{\sigma^{tot}}+\boldsymbol{b}=0 \tag{73}
$$

where $\boldsymbol{\sigma^{tot}}$ and $\boldsymbol{b}$ stand for the total stresses and the body forces at a certain point of the domain, respectively. The body forces are usually due to the self-weight which is related to the density. For unsaturated soil, the bulk density can be estimated as:

$$
\rho^b=nS^g\rho^g+nS^l\rho^l+(1-n)\rho^s \tag{74}
$$

By defining the net stress $\boldsymbol{\sigma}$ as the difference between total stress $\boldsymbol{\sigma}^{tot}$ and the fluid pressure P_i, where $i=g$ in unsaturated state and $i=l$ at full saturation with suction = 0 (here, the net stress becomes equal to the Terzaghi's effective stress), Eq. (73) is exploited to derived the following incremental virtual work equilibrium equation over domain Ω [43,44]:

$$
\int_\Omega\delta\boldsymbol{\varepsilon}^T\delta\boldsymbol{\sigma}d\Omega+\int_\Omega\delta P_i\boldsymbol{m}^T\delta\boldsymbol{\varepsilon}d\Omega=\delta\boldsymbol{f_u} \tag{75}
$$

with $\boldsymbol{m}=\{1,1,1,0,0,0\}$, $\boldsymbol{\varepsilon}$ is the strain vector and

$$
\delta\boldsymbol{f_u}=\int_\Omega\delta\boldsymbol{u}\delta\boldsymbol{b}d\Omega+\int_\Gamma\delta\boldsymbol{u}\delta\boldsymbol{t}d\Gamma \tag{76}
$$

The force vector $\delta\boldsymbol{f_u}$ describes the increment in body forces $\delta\boldsymbol{b}$ and the traction forces $\delta\boldsymbol{t}$ being applied on the domain boundaries Γ. The symbol $\delta\boldsymbol{u}$ represents the vector of increment displacement which can be linked to the displacements at the finite element nodes $\hat{\boldsymbol{u}}$ using the shape functions $\boldsymbol{N}_b$ as $\delta\boldsymbol{u}=\boldsymbol{N}_b\delta\hat{\boldsymbol{u}}$. By employing a suitable stress-strain relationship $\delta\boldsymbol{\sigma}=\boldsymbol{M}\delta\boldsymbol{\varepsilon}$ and correlating the strain to the nodal displacements through the kinematic relationship $\delta\boldsymbol{\varepsilon}=\nabla\boldsymbol{N}_b\delta\hat{\boldsymbol{u}}$, the discretised finite element form of Eq. (75) reads:

$$
\begin{aligned}
&\int_\Omega(\nabla\boldsymbol{N}_b)^T\boldsymbol{M}\nabla\boldsymbol{N}_b\delta\hat{\boldsymbol{u}}d\Omega+\int_\Omega(\boldsymbol{N}_b)^T\rho_w^l g\boldsymbol{m}^T\nabla\boldsymbol{N}_b\delta\hat{\boldsymbol{h}}_i d\Omega\\
&\quad=\int_\Omega\boldsymbol{N}_b\delta\boldsymbol{b}d\Omega+\int_\Gamma\boldsymbol{N}_b\delta\boldsymbol{t}d\Gamma
\end{aligned}
\tag{77}
$$

where $\boldsymbol{M}$ denotes the material stiffness matrix and $\hat{\boldsymbol{h}}_i$ is the fluid pressure head at the finite element nodes. Eq. (77) shows that any change in the applied external tractions, the soil self-weight, the applied suction, the temperature or the applied fluid pressure will affect the balance and leads to a displacement increment. While the external tractions are prescribed values, an independent procedure is required to evaluate the suction, fluid pressure and temperature variation over time. That is achieved by the coupled solution of Eqs. (49), (61), (71) and (73). The soil response to the applied force represented by the material stiffness matrix $\boldsymbol{M}$ is heavily dependent on the applied stress-strain relationship, due to:

$$
\int_\Omega\boldsymbol{M}\nabla\boldsymbol{N}_b\delta\hat{\boldsymbol{u}}d\Omega=\int_\Omega\delta\boldsymbol{\sigma}d\Omega \tag{78}
$$

which also shows that a stress integration over a load step should be performed during mechanical balance calculations by employing a suitable constitutive model and numerical stress integration technique. In this paper, a slightly modified version of the well-known Barcelona Basic Model (BBM) is adopted [45–47]. The modification is introduced to account for the thermal effects and the dependency of the elastic parameters on suction and net stress. Both implicit [48–50] and explicit scheme with error control [51–55] could be used to integrate the constitutive stresses. In what follows, only the mathematical formulation of the constitutive model is presented whereas the numerical integration details are omitted due to space limitations.

2.3.1. BBM with thermal effects

The elastoplastic Barcelona Basic Model [9] is based on the Modified Cam Clay model [56], and can be viewed as its extension which accounts for unsaturated soil behaviour. BBM uses net stress $\boldsymbol{\sigma}=\boldsymbol{\sigma}^{tot}-\boldsymbol{m}^T P_g$ and suction $s=\rho_w^l g\psi$ as the independent stress variables. At full saturation, the net stresses are replaced by the effective stress definition $\boldsymbol{\sigma}=\boldsymbol{\sigma}^{tot}-\boldsymbol{m}^T P_l$ with $s=0$ and P_l is the pore-water pressure. Potential numerical difficulties upon transition from unsaturated soil state to the full saturation are reported in literature [39,57]. Wheeler et al. [58] showed that for a certain combination of parameters, BBM yield surface might suffer non-convexity and consequently higher possibility for numerical complication near saturation. However, we have not encountered any problems thus far related to transition between saturated and unsaturated regimes, possibly due to the choice of time-stepping scheme. Should any numerical problems related to the transition between saturated and unsaturated regimes be observed, algorithmic solutions are available [39,57].

The presented formulation currently uses total stresses and suction, as opposed to the effective stresses. As indicated in [59,60],

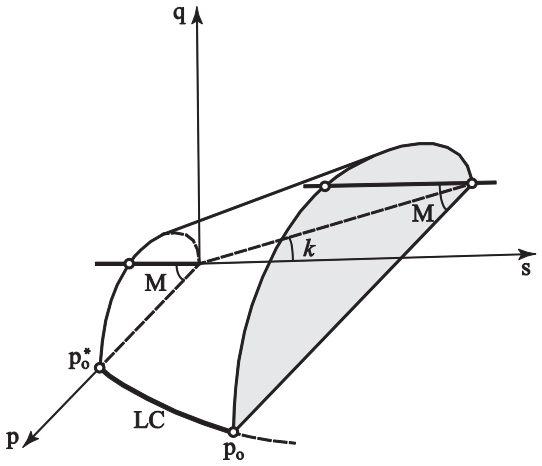

Fig. 2. 3D representation of the yield surface in BBM at a constant temperature.

formulations based on the effective stress or the total stress are equivalent. As such the use of total stress may be viewed as a matter of preference. Furthermore, the presented framework may easily accommodate constitutive models formulated in terms of effective stress using the transition technique given by [59,60].

2.3.1.1. BBM in elasticity. The rate of total strain $\dot{\boldsymbol{\varepsilon}}$ in BBM is decomposed into the elastic $\dot{\boldsymbol{\varepsilon}}_e$ and the plastic part $\dot{\boldsymbol{\varepsilon}}_p$:

$$\dot{\boldsymbol{\varepsilon}} = \dot{\boldsymbol{\varepsilon}}_e + \dot{\boldsymbol{\varepsilon}}_p \tag{79}$$

The rate of the elastic strain $\dot{\boldsymbol{\varepsilon}}_e$ is decomposed further into the elastic strain rate due to the net stress, $\dot{\boldsymbol{\varepsilon}}_e^{\sigma}$, the elastic strain rate related to the suction change $\dot{\boldsymbol{\varepsilon}}_e^{s}$ and the elastic strain rate due to thermal effects $\dot{\boldsymbol{\varepsilon}}_e^{T}$. It is assumed that suction and temperature introduce only volumetric deformations:

$$\dot{\boldsymbol{\varepsilon}}_e = \dot{\boldsymbol{\varepsilon}}_e^{\sigma} + \boldsymbol{m}^T \dot{\varepsilon}_e^{s} + \boldsymbol{m}^T \dot{\varepsilon}_e^{T} \tag{80}$$

Thus, the elastic net stress rate can be calculated as:

$$\dot{\boldsymbol{\sigma}} = \boldsymbol{D}^e \dot{\boldsymbol{\varepsilon}}_e^{\sigma} = \boldsymbol{D}^e \left(\dot{\boldsymbol{\varepsilon}} - \boldsymbol{m}^T \dot{\varepsilon}_e^{s} - \boldsymbol{m}^T \dot{\varepsilon}_e^{T}\right) \tag{81}$$

where $\boldsymbol{D}^e$ is the elastic stiffness matrix

$$\boldsymbol{D}^e = \begin{bmatrix} K+4/3G & K-2/3G & K-2/3G & 0 & 0 & 0 \\ & K+4/3G & K-2/3G & 0 & 0 & 0 \\ & & K+4/3G & 0 & 0 & 0 \\ & & & G & 0 & 0 \\ & sym & & & G & 0 \\ & & & & & G \end{bmatrix} \tag{82}$$

with

$$K = \frac{\upsilon p}{\kappa}; \quad G = \frac{3K(1-2\nu)}{2(1+\nu)} \tag{83}$$

In the above formulation K and G are the bulk and the shear modulus respectively, υ stands for the soil specific volume, κ for the soil swelling index, ν is the Poisson's ratio and $p = \mathrm{tr}(\boldsymbol{\sigma})/3$ is the mean (isotropic) net pressure. The strain rate is related to the suction change via

$$\dot{\varepsilon}_e^{s} = \frac{\kappa_s \dot{s}}{3\upsilon(s + P_{atm})}, \tag{84}$$

where P_{atm} is the atmospheric pressure and κ_s is the soil swelling index with respect to the suction variation. In order to account for the swelling nature of some soils, the elastic stiffness is made pressure dependent as follows [27]:

$$\begin{aligned} \kappa &= \kappa_o(1 + \alpha_\kappa s) \\ \kappa_s &= \kappa_{so}\left[1 + \alpha_{\kappa s1} \ln\left(\frac{p}{p_{ref}^c}\right)\right] e^{\alpha_{\kappa s2} s} \end{aligned} \tag{85}$$

where κ_o and κ_{so} are reference values of κ and κ_s, respectively. The value of κ_s is assumed to be equal to κ_{so} as long as $p < p_{ref}^c$, otherwise Eq. (85) applies. At very high suction, the value of κ may show unrealistic negative values depending on α_κ value. To avoid this possibility, a minimum value of $\kappa = 0.001\kappa_o$ is assumed. Finally, theses parameters are only used during elastic calculations while Eqs. (92) and (101) utilize the reference value $\kappa = \kappa_o$. The temperature variation introduces elastic strain [61,10,62]

$$\dot{\varepsilon}_e^{T} = \frac{(\alpha_o + \alpha_2(T - T_o))\dot{T}}{3} \tag{86}$$

In Eqs. (85) and (86), the parameters α_κ, $\alpha_{\kappa s1}$, $\alpha_{\kappa s2}$, p_{ref}^c, α_o and α_2 are material constants. They are responsible for the elastic response of the material to any change in suction, net stress, or temperature.

2.3.1.2. BBM in plasticity. As depicted by Fig. 2, a 3D representation of the yield surface of BBM is

$$F = q^2 - M^2(p + p_s)(p_o - p) = 0 \tag{87}$$

where M is the slope of critical state line and q stands for the deviatoric stress:

$$q = \frac{1}{\sqrt{2}}\sqrt{(\sigma_1 - \sigma_2)^2 + (\sigma_2 - \sigma_3)^2 + (\sigma_3 - \sigma_1)^2}, \tag{88}$$

where σ_1, σ_2 and σ_3 are the principal stresses. The trace of the yield surface in the plane $q = 0$ is the *Loading Collapse* (LC) curve. The plastic strain direction is determined using a plastic potential function

$$Q = \alpha q^2 - M^2(p + p_s)(p_o - p) = 0 \tag{89}$$

The factor α which allows for the recovery of the Jaky's approximation [63] of coefficient of at rest soil pressure K_0 in 1D compression, is defined as

$$\alpha = \frac{M(M-9)(M-3)}{9(6-M)} \frac{\lambda}{\lambda - \kappa}, \tag{90}$$

where λ is the slope of normal consolidation line.

Extended BBM assumes, see Fig. 3, that the soil shear strength is affected by suction and temperature as follows [10]

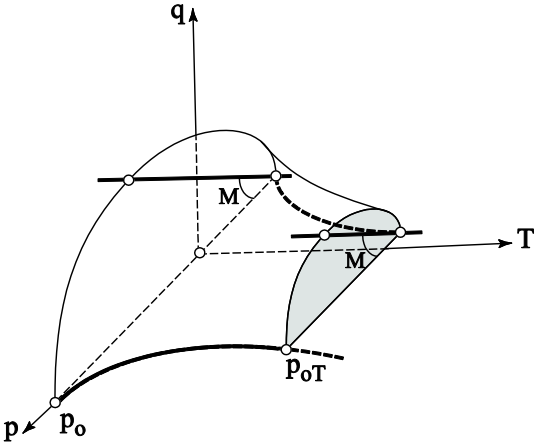

Fig. 3. 3D representation of the yield surface in BBM at a constant suction and varying temperature.

$$p_s = k s e^{-\rho^T \Delta T}, \tag{91}$$

where ρ^T and k are material constants. The soil preconsolidation pressure p_o is also considered to be suction and temperature dependent through the equation [10]

$$p_o = p^c \left(\frac{p_{oT}^*}{p^c}\right)^{\frac{\lambda - \kappa}{\lambda_s - \kappa}} \tag{92}$$

with

$$\lambda_s = \lambda\left[(1-r)e^{-\beta s} + r\right] \tag{93}$$

and

$$p_{oT}^* = p_o^* + 2(\alpha_1 \Delta T + \alpha_3 \Delta T |\Delta T|), \tag{94}$$

where the preconsolidation pressure at full saturation and a reference temperature T_o = 20 °C is indicated by p_o^*. Eqs. (92)–(94) introduce p^c, β, r, α_1 and α_3 as new BBM parameters. These parameters are used to define the effect of suction and temperature on the preconsolidation pressure and the post-yielding stiffness. Alternatively, [64] proposes the following equation to describe the temperature effect on saturated preconsolidation pressure:

$$p_{oT}^* = p_o^*\left(1 - \gamma_T \log\left(\frac{T - T_{ref}}{T_o - T_{ref}}\right)\right) \tag{95}$$

where γ_T is a material constant. The above equation is more practical compared to Eq. (94), as it reduces the number of required parameters by one. However, Eq. (94) has slightly more flexibility in fitting the experimental data. Both equations are implemented in the current code.

The theoretical frameworks proposed by [10,64] are employed in order to include thermal effects. The net stress rate is

$$\dot{\boldsymbol{\sigma}} = \boldsymbol{D}^e \dot{\boldsymbol{\varepsilon}}_e^\sigma = \boldsymbol{D}^e\left(\dot{\boldsymbol{\varepsilon}} - \boldsymbol{m}^T \dot{\varepsilon}_s^e - \boldsymbol{m}^T \dot{\varepsilon}_T^e - \dot{\boldsymbol{\varepsilon}}_p\right) \tag{96}$$

The plastic strain rate $\dot{\boldsymbol{\varepsilon}}_p$ is determined by the flow rule,

$$\dot{\boldsymbol{\varepsilon}}_p = \dot{\Lambda}\frac{\partial Q}{\partial \boldsymbol{\sigma}} \tag{97}$$

The plastic multiplier $\dot{\Lambda}$ is derived based on plasticity theory,

$$\dot{\Lambda} = \frac{\boldsymbol{a}^T \boldsymbol{D}^e \dot{\boldsymbol{\varepsilon}} + \left[c_1 - \boldsymbol{a}^T \boldsymbol{D}^e \boldsymbol{b}_1\right]\dot{s} + \left[c_2 - \boldsymbol{a}^T \boldsymbol{D}^e \boldsymbol{b}_2\right]\dot{T}}{\boldsymbol{a}^T \boldsymbol{D}^e \boldsymbol{g} - d}, \tag{98}$$

where

$$\begin{aligned} \boldsymbol{a} &= \frac{\partial F}{\partial \sigma}; \quad \boldsymbol{b}_1 = \boldsymbol{m}\left(\frac{\kappa_s}{3v(s+P_{atm})}\right); \quad \boldsymbol{b}_2 \\ &= \boldsymbol{m}\left(\frac{-(\alpha_o + \alpha_2 \Delta T)}{3}\right); \quad c_1 = \frac{\partial F}{\partial s}; \quad c_2 = \frac{\partial F}{\partial T}; \quad d \\ &= \frac{\partial F}{\partial \varepsilon_p^v}\boldsymbol{m}^T \cdot \frac{\partial Q}{\partial \boldsymbol{\sigma}}; \quad \boldsymbol{g} = \frac{\partial Q}{\partial \boldsymbol{\sigma}} \end{aligned} \tag{99}$$

Substituting Eqs. (84), (86) and (97) into Eq. (96) yields the net stress rate:

$$\begin{aligned} \dot{\boldsymbol{\sigma}} = \boldsymbol{D}^e \dot{\boldsymbol{\varepsilon}} - \boldsymbol{D}^e \boldsymbol{m}^T \frac{\kappa_s}{3v(s+P_{atm})}\dot{s} + \boldsymbol{D}^e \boldsymbol{m}^T \frac{(\alpha_o + \alpha_2 \Delta T)}{3}\dot{T} \\ - \boldsymbol{D}^e \dot{\Lambda}\frac{\partial Q}{\partial \boldsymbol{\sigma}} \end{aligned} \tag{100}$$

Finally, the preconsolidation pressure is updated like:

$$p_o^* = p_{oi}^* e^{\frac{v\varepsilon_p^v}{\lambda - \kappa}}, \tag{101}$$

where p_{oi}^* is the initial preconsolidation pressure and $\dot{\varepsilon}_p^v = \mathrm{tr}(\dot{\boldsymbol{\varepsilon}}_p)$ is the plastic volumetric strain rate.

3. Numerical implementation

The previously described balance equations (49), (61), (71) and (73) are discretised using the finite element method [3,4,7,8,28,41,65–70], transforming them into an equivalent system of first-order ordinary differential equations:

$$\begin{aligned} &\begin{bmatrix} \boldsymbol{M}_{uu} & \boldsymbol{M}_{wu} & \boldsymbol{M}_{gu} & 0 \\ \boldsymbol{M}_{uw} & \boldsymbol{M}_{ww} & \boldsymbol{M}_{gw} & \boldsymbol{M}_{Tw} \\ \boldsymbol{M}_{ug} & \boldsymbol{M}_{wg} & \boldsymbol{M}_{gg} & \boldsymbol{M}_{Tg} \\ \boldsymbol{M}_{uT} & \boldsymbol{M}_{wT} & \boldsymbol{M}_{gT} & \boldsymbol{M}_{TT} \end{bmatrix} \begin{bmatrix} \delta\widehat{\boldsymbol{u}} \\ \delta\widehat{\boldsymbol{h}}_w \\ \delta\widehat{\boldsymbol{h}}_g \\ \delta\widehat{\boldsymbol{T}} \end{bmatrix} + \begin{bmatrix} 0 & 0 & 0 & 0 \\ 0 & \boldsymbol{K}_{ww} & \boldsymbol{K}_{gw} & \boldsymbol{K}_{Tw} \\ 0 & \boldsymbol{K}_{wg} & \boldsymbol{K}_{gg} & \boldsymbol{K}_{Tg} \\ 0 & \boldsymbol{K}_{wT} & \boldsymbol{K}_{gT} & \boldsymbol{K}_{TT} \end{bmatrix} \begin{bmatrix} \widehat{\boldsymbol{u}} \\ \widehat{\boldsymbol{h}}_w \\ \widehat{\boldsymbol{h}}_g \\ \widehat{\boldsymbol{T}} \end{bmatrix} \\ &= \begin{bmatrix} \delta\boldsymbol{f}_u \\ \boldsymbol{f}_w \\ \boldsymbol{f}_g \\ \boldsymbol{f}_T \end{bmatrix} \end{aligned} \tag{102}$$

where the terms $\boldsymbol{M}_{ij}$, $\boldsymbol{K}_{ij}$ and $\boldsymbol{f}_j$ are given in the Appendix B. The symbols $\widehat{\boldsymbol{T}}, \widehat{\boldsymbol{h}}_w, \widehat{\boldsymbol{h}}_g$ and $\widehat{\boldsymbol{u}}$ represent the nodal values of the unknown temperature, water pressure head, gas pressure head, and displacements, respectively. Assuming that these unknowns are stored in $\boldsymbol{X} = \left\{\widehat{\boldsymbol{u}}, \widehat{\boldsymbol{h}}_w, \widehat{\boldsymbol{h}}_g, \widehat{\boldsymbol{T}}\right\}$, the above system of equations is

$$\boldsymbol{M}\dot{\boldsymbol{X}} + \boldsymbol{K}\boldsymbol{X} = \boldsymbol{F} \tag{103}$$

This equation may be discretised over time using finite differences, yielding a system of nonlinear algebraic equations which may be solved, for example, by using Newton-Raphson iterations. Knowing the initial conditions at time step i, the residual $\boldsymbol{R}^{i+1}$ at the time step $i+1$ is

$$\boldsymbol{R}^{i+1} = \boldsymbol{M}^{i+1}\frac{\boldsymbol{X}^{i+1} - \boldsymbol{X}^i}{\Delta t} + \boldsymbol{K}^{i+1}\boldsymbol{X}^{i+1} - \boldsymbol{F}^{i+1} \tag{104}$$

The solution is considered to be converged once the Euclidean norm of the residual is reduced below a desired tolerable error $\|\boldsymbol{R}\| < Tol$. This is accomplished by iterative improvement of the solution,

$$\boldsymbol{X}_{j+1}^{i+1} = \boldsymbol{X}_j^{i+1} - \boldsymbol{A}_{j+1}^{i+1} \cdot \boldsymbol{R}_{j+1}^{i+1}, \tag{105}$$

where A_{j+1}^{i+1} is the Jacobian of the system at time step $i+1$ and iteration $j+1$

$$\boldsymbol{A}_{j+1}^{i+1} = \frac{\partial \boldsymbol{R}_{j+1}^{i+1}}{\partial \boldsymbol{X}_{j+1}^{i+1}} \tag{106}$$

The global error tolerance of $Tol = 10^{-4}$ which applies for every residual in the solved system, is used for the purposes of this study. This formulation is implemented into a FE code using NUMERRIN numerical solver [68]. The implementation includes special logical switches coded which allows to choose the balance equations to be coupled in Eq. (102) and used in the subsequent formation of residuals in Eq. (104). For example, if the problem is isothermal, energy balance Eq. (71) is not solved and no corresponding residual is formed. In such a case the temperature has a constant value in the whole solution domain equal to the initial temperature. In the remainder of this paper, the implemented code is referred to as "Aalto Code". The following sections illustrate numerical results that are generated using Aalto Code and compared to known analytical solutions and experimental data.

4. Verification and validation of the implemented code

As a general rule, the finite element mesh in each example is first subjected to a convergence study and refined accordingly to avoid any visible dependency of the numerical results on the num-

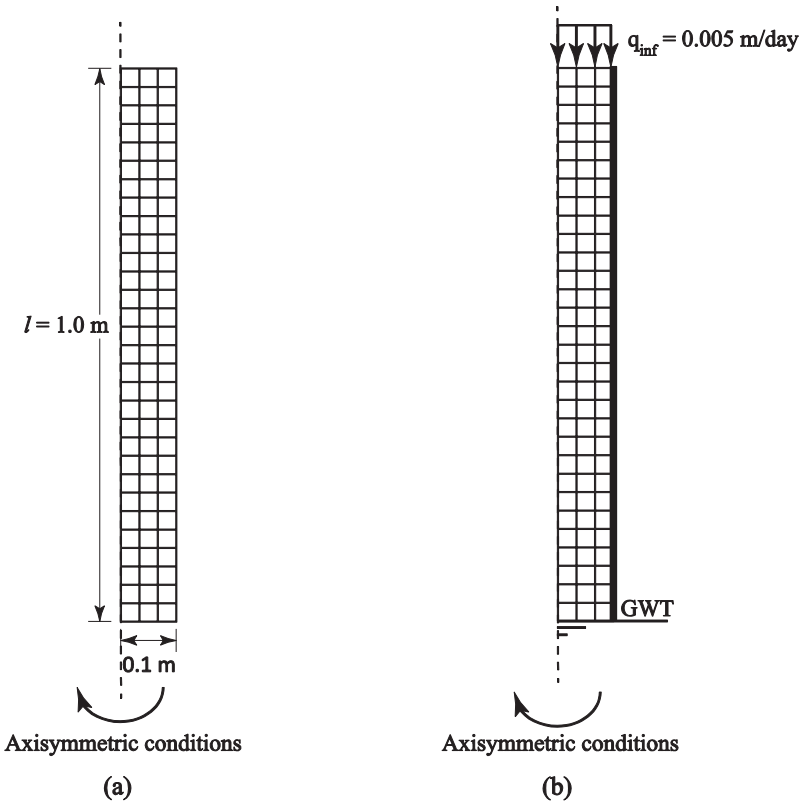

Fig. 4. One dimensional infiltration problem: (a) FE model; (b) hydraulic boundary conditions.

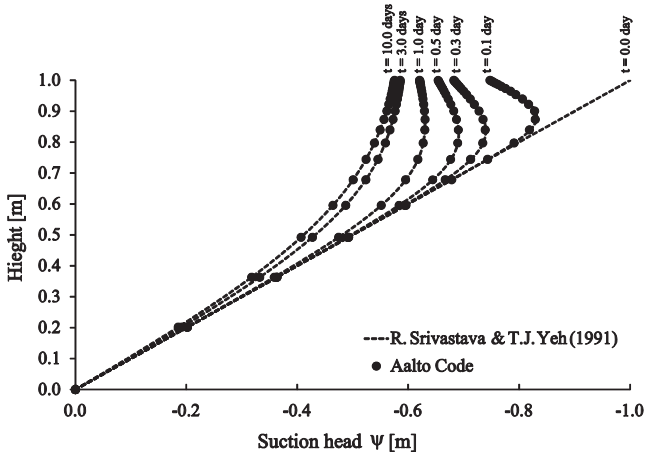

Fig. 5. Numerical results versus analytical solution for 1D infiltration.

ber of elements or the time step size. The results shown here mainly concentrate on the validation of coupled phenomena. Extra verifications related e.g. to the mechanical model can be found in [55].

4.1. Verification: uncoupled one dimensional infiltration

Srivastava and Yeh [71] derived an uncoupled analytical solution for Eq. (49) for the case of one dimensional infiltration into a soil with particular relative permeability and water retention curves of the forms:

$$K^l = K^l_{sat} e^{-\xi\psi} \tag{107}$$

$$S^l = \left(S^l_{sat} - S^l_{res}\right) e^{-\xi\psi} + S^l_{res} \tag{108}$$

where ξ is a soil parameter. Based on [71], a soil layer with a total height of l and an initial hydrostatic suction profile exposed at the top to an infiltration rate q_{inf}, has suction head ψ at an elevation z and time t equal to:

$$\psi(z,t) = \frac{1}{\xi}\ln(B) \tag{109}$$

where

$$B = \frac{q_{inf}}{K^l_{sat}} - \left(\frac{q_{inf}}{K^l_{sat}} - 1\right) e^{-z^*} - \frac{4q_{inf}}{K^l_{sat}} e^{\frac{(l^*-z^*)}{2}} e^{-\frac{t^*}{4}} \sum_{i=1}^{\infty} \frac{\sin(\lambda_i z^*)\sin(\lambda_i l^*) e^{-\lambda_i^2 t^*}}{1 + \left(\frac{l^*}{2}\right) + 2\lambda_i^2 l^*}, \tag{110}$$

$$t^* = \frac{\xi K^l_{sat} t}{n\left(S^l_{sat} - S^l_{res}\right)}, \quad z^* = \xi z, \quad l^* = \xi l \tag{111}$$

In the above solution λ_i represents the i^{th} root of the characteristic equation:

$$\tan(\lambda l^*) + 2\lambda = 0 \tag{112}$$

A soil with a saturated permeability of $K^l_{sat} = 0.1$ m/day and $\xi = 5.0$ [1/m] is used to generate the numerical results. The residual and saturated degrees of saturation are $S^l_{res} = 0.23$ and $S^l_{sat} = 1.0$, respectively. For the purposes of this example, only the mass balance equation of water component is used in Eq. (102) and the subsequent formation of residuals in Eq. (104). The temperature is kept constant at 20 °C throughout the solution time with atmospheric gas pressure, minimal initial stress of 1.0 kPa

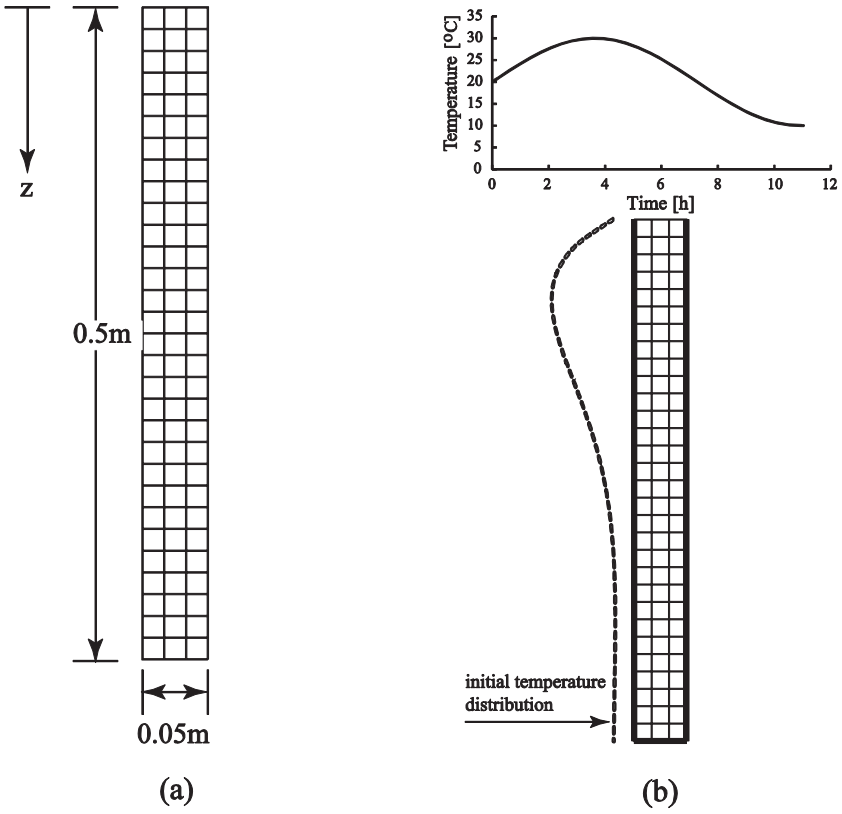

Fig. 6. One dimensional heat flow problem: (a) FE model; (b) thermal boundary conditions.

Table 1
Used parameters in the 1D heat flow example.

λ_T [W/m/K]	c_s [J/kg/K]	c_w [J/kg/K]	n	ρ^s [kg/m^3]	ρ_w^l [kg/m^3]	$\overline{T}$ [°C]	A_o [°C]	ω [1/s]
1.0	1000.0	4180.0	0.4	2650.0	1000.0	20.0	10.0	0.00012

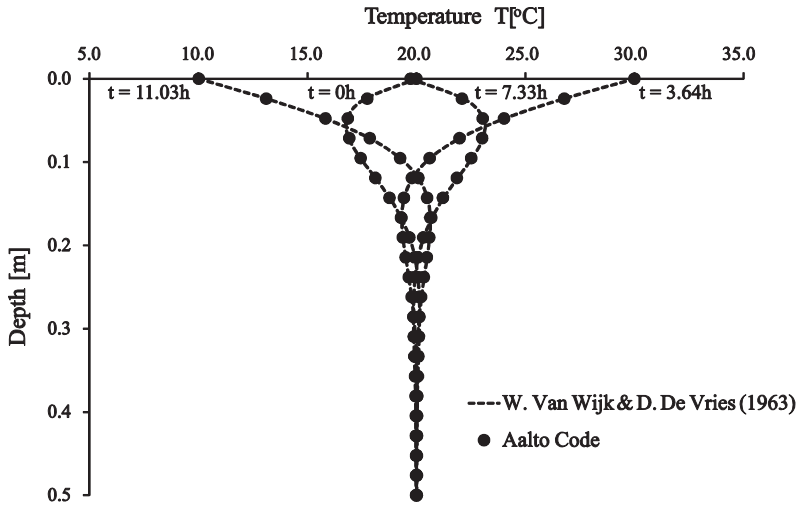

Fig. 7. Numerical results versus analytical solution for 1D heat flow.

and a constant porosity $n = 0.4$. On top of that, for this particular case of 1D infiltration test, Eqs. (107) and (108) are used instead of Eqs. (25) and (20) to represent the relative permeability curve and soil water retention curve of the soil.

Fig. 4 describes the mesh and boundary conditions used in this verification example. The vertical hydraulic boundaries are impermeable, to represent 1D conditions. An infiltration rate of $q_{inf} = 0.005$ m/day is applied at the top boundary of the domain while a ground water table is located at 1.0 m below ground surface, modelled by imposing a zero water head at the bottom boundary. Fig. 5 shows an excellent agreement between the numerical results and the analytical solution for this particular problem.

Fig. 8. CIEMAT infiltration cells [73].

4.2. Verification: uncoupled one dimensional heat flow

On neglecting coupling effects and vapour flow, the energy balance Eq. (71) reduces to the following form in one dimensional case:

$$c\frac{\partial T}{\partial t} - \nabla \cdot \boldsymbol{q}^T = 0 \tag{113}$$

with the volumetric soil heat capacity $c = (1-n)\rho^s c_s + n\rho_w^l c_w$ for saturated soil. By assuming a constant soil thermal conductivity λ_T and a constant volumetric soil heat capacity, Van Wijk and De Vries [72] gave the following analytical solution for one dimensional heat flow:

$$T(z,t) = \overline{T} + A_o e^{-z\sqrt{\frac{\omega c}{2\lambda_T}}} \sin\left(\omega t - z\sqrt{\frac{\omega c}{2\lambda_T}}\right), \tag{114}$$

where $T(z,t)$ is the soil temperature at depth z and time t. This solution is valid only for the boundary conditions with a sinusoidally varying temperature at the soil surface:

$$T(t) = \overline{T} + A_o \sin(\omega t) \tag{115}$$

The initial temperature can be easily derived from Eq. (114) by assuming $t = 0$. In the above equations $\overline{T}$ represents the average temperature over time while A_o and ω are the amplitude and the radial frequency, respectively. The used numerical model to solve this problem is shown in Fig. 6. It represents a soil layer of thickness 0.5 m being subjected to a temperature variation at its surface. Closed thermal boundary conditions are assumed to recover the one dimensional conditions as it is clear in Fig. 6(b). The soil properties and thermal load parameters employed in this verification example are listed in Table 1. The analysis in this example is uncoupled, in the sense that only the energy balance equation is solved. The numerical results for temperature profile at different time steps are in excellent agreement with the analytical solution as it is shown in Fig. 7.

4.3. Validation of coupled THM behaviour: infiltration tests using FEBEX bentonite

Villar et al. [73] performed two hydration tests on FEBEX bentonite using cylindrical cells with an inner diameter of 0.07 m and a useful height of 0.4 m. The cells are made of Teflon PTFE in order to ensure maximum lateral thermal insulation. Additionally, the cells are externally surrounded by semi-cylindrical steel pieces to prevent the developed swelling pressure of the bentonite from causing any deformation of the cells (see Fig. 8). The bentonite in the cells had been statically compacted with an average com-

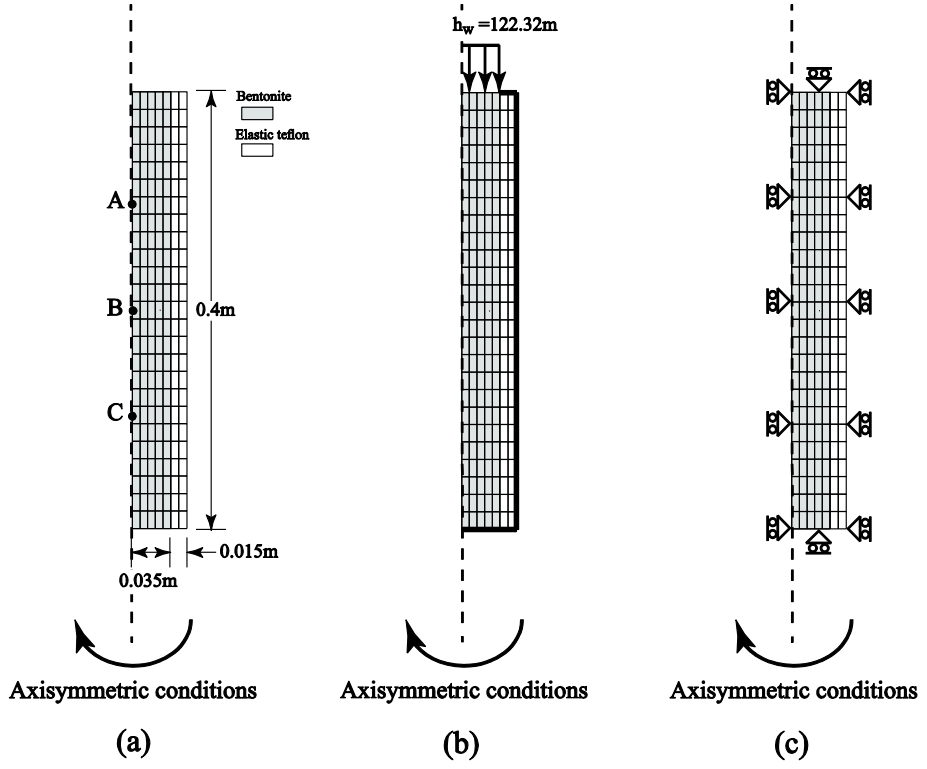

Fig. 9. Finite element model for isothermal infiltration test: (a) dimensions and control points locations; (b) hydraulic boundary conditions; (c) mechanical boundary conditions.

Table 2
Teflon, steel and foam properties.

Material	E [kPa]	ν	λ_T [W/m/K]
Teflon	5.0E+5	0.46	0.25
Steel	2.0E+8	0.3	12.0
Foam	1.0E+4	0.3	0.17

paction pressure of 30 MPa with an initial gravimetric water content of around 0.13–0.14 and initial nominal dry density of 1650 kg/m^3. In the first test (I40), bentonite was hydrated from the upper end of the cell under isothermal conditions. Similarly, the bentonite in the second test (GT40) was hydrated but under a thermal gradient with bottom of the specimen subjected to a maximum constant temperature of 100 °C.

For the non-isothermal test, the hydration was performed after 65 h of heating at which point the temperature of the column became stable. A cooling system was used in order to ensure constant temperature at the upper end. The measurements are provided in form of temperature and relative humidity distribution in time at specific positions along the sample height (Point A at $z = 0.3$ m, Point B at $z = 0.2$ m and Point C at $z = 0.1$ m) (see Fig. 10(a)). No measurements of deformations or stresses are recorded for these tests. In both cases hydration is performed using low salinity water at a pressure of 1.2 MPa. These tests have been modelled previously [75–77], and as such an excellent references for the expected numerical performance and potential modelling problems exist.

4.3.1. Finite element model and material parameters

Regarding the isothermal case, the finite element mesh consists of 175 quadrilateral 4-noded elements with four stress integration points per element as depicted in Fig. 9(a). The bentonite is modelled as a BBM material accounting for thermal effects (see Section 2.3.1), whereas the Teflon surrounding the sample is modelled as a non-porous and linear-elastic material with an elasticity modulus of $E = 500.0$ MPa and Poisson's ratio of $\nu = 0.46$ [78]. The modelled domain is initially considered to be stress free with a minimal principal net stress of 1.0 kPa. The hydraulic and mechanical boundary conditions are illustrated in Fig. 9 (b) and (c). Note that the sample boundaries are not allowed to move, and thus the volume is constant. A similar configuration is used to model the non-isothermal infiltration test; however, more details must be included in the finite element model to better capture the thermal effects. In addition to the Teflon, the supporting steel and isolation foam are explicitly modelled, in this case assuming a non-porous linear elastic behaviour but with different mechanical and thermal properties (see Table 2).

The used thermal properties of these materials are calibrated based on the measured temperature. Care is taken to ensure these values remain within acceptable physical ranges, and is achieved for steel and Teflon. However, the foam layer is assigned a slightly out-of-range value in order to correctly capture the thermal loss at the outer boundary of the sample. In Fig. 10 the FE model and boundary conditions utilized in the non-isothermal conditions are illustrated. In this case, the finite element mesh consists of 250 quadrilateral 4-noded elements. The initial temperature is prescribed at 22.0 °C and remains constant at the boundaries other than the bottom of the bentonite sample which is subjected to 100.0 °C throughout the test. The thermal boundary conditions are illustrated in Fig. 10(c). The soil water retention data given by [74] are fitted using the van Genuchten formula [23] with the parameters $g_{\alpha o} = 12.0\text{E}-4[1/\text{m}]$, $g_{no} = 1.22$, $S^l_{res} = 0.01$ and $S^l_{sat} = 1.0$, leading to an acceptable match of the experimental data (see Fig. 11). The fitting also yields parameters $\xi^T_n = -1.0\text{E}-4[1/\text{K}]$ and $\xi^T_w = -1.5\text{E}-3[1/\text{K}]$, taking into account the effect of temperature on the soil water characteristic curve as explained in Section 2.1.2.2. The initial gravimetric water content of 0.14 corresponds to an initial degree of saturation of $S^l_w = \frac{\omega G_s}{e} = \frac{0.14\times 2.7}{0.677} \approx 0.56$ which correlates to the initial suction head of $\psi = 12000.0$ m, see Fig. 11. The initial gas pressure is assumed to be atmospheric. The top boundary is kept open to atmospheric pressure throughout the simulation, while all other

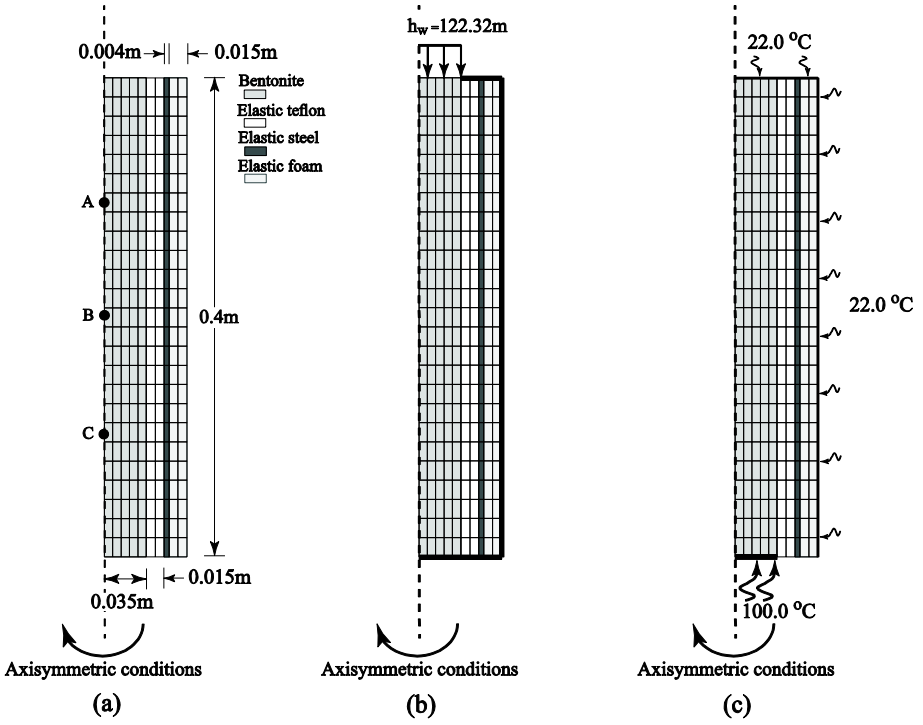

Fig. 10. Finite element model for non-isothermal infiltration test: (a) dimensions and control points locations; (b) hydraulic boundary conditions; (c) thermal boundary conditions.

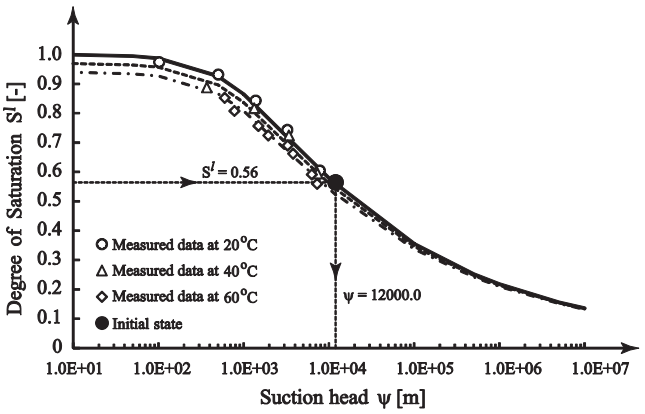

Fig. 11. Used soil water retention curve, fitted at different temperatures. Experimental data are after [74].

boundaries are treated as closed flow-boundaries for gas. The other parameters used in the analyses were taken from literature [27,61] and are given in Table 3. In the simulations, the relative permeability curve is described by Eq. (25). The thermal conductivity of bentonite is averaged according to the following empirical correlation [79]

$$\lambda_T = \lambda_{sat}^{S^l} \lambda_{dry}^{S^g} \tag{116}$$

The temperature variations have substantial effect on the development of gas pressure. Due to the fact that no temperature changes are involved in the isothermal test, the gas pressure remains constant at its applied initial atmospheric value, without solving its corresponding balance equation (61). However, the dry air mass balance equation is solved for the case of the non-isothermal infiltration test. Unfortunately, no measurements have been recorded for gas pressure values throughout the test, and as such the model predictions for gas pressure cannot be easily validated.

4.3.2. Discussion of numerical results

4.3.2.1. Isothermal infiltration. The measured relative humidity at points A, B and C is depicted in Fig. 12. The figure also shows the calculated relative humidity values using the fully-coupled HM option in Aalto Code. The quantitative agreement between measured and calculated results validates the implementation against a well-documented experimental data. A further verification of the results is sought by comparing the numerical results to that produced by CODE_BRIGHT [11], a well-established fully coupled THM code. The almost perfect agreement between Aalto Code and CODE_BRIGHT results as it clear in Fig. 12 gives more confidence about the correctness of the implementation in case of HM coupling. To illustrate the effect of mechanical coupling on the flow field, the numerical test is repeated with free-swelling conditions, whereby the top mechanical constraint is removed. Fig. 13 indicates relatively faster hydration in the case of the constant volume conditions. That can be related to the progressive reduction in soil porosity due to the mechanical constraint at the top boundary.

4.3.2.2. Non-isothermal infiltration. Using exactly the same materials properties, the numerical non-isothermal infiltration test produces results shown in Fig. 14 for variations in relative humidity and Fig. 15 for variations in temperature. The figures indicate good qualitative agreement between the experimental data and the numerical simulations. However, quantitatively the code seems to predict better temperature distribution if compared to the prediction of relative humidity over time. Fig. 14 also illustrates the noticeable impact of thermal effects on water retention, especially when the temperature gradient is high. Note that it is not possible for this example to use CODE_BRIGHT for verification purposes, as it uses a different approach and assumptions; vapour flow in CODE_BRIGHT is based on Fick's law for diffusion [31,80], which is simpler compared to the implemented model by Philip and De Vries [33].

Similarly to experiences of other researchers [76,77,81], the numerical predictions of relative humidity degrades by deviating progressively from the measurements with the development of the test time, see Fig. 14. Among other unsolved problems, this faster numerical hydration triggers the need for a deeper revision of the assumptions used, both in terms of the mechanical behaviour and multiphase flow formulations. For example, taking into account a decrease in the hydraulic conductivity in swelling soil due to the absorbed water in pore space [76,82,83], the hydraulic conductivity formula (25) can be extended to:

$$K^l = K_{sat}^l \left(\frac{S^l - S_{res}^l}{S_{sat}^l - S_{res}^l} \right)^3 \left(1 - S_{abs}^l \right) \tag{117}$$

where S_{abs}^l is the absorbed portion of degree of saturation being related to the degree of saturation S^l through a factor α_{swell} following [76]:

Table 3
FEBEX bentonite properties as used in the CIEMAT infiltration tests.

(a) Mechanical properties

ν	κ_o	κ_{so}	n	α_o [1/K]	α_1	α_2	α_3	α_k	α_{ks1}	α_{ks2}
0.4	0.05	0.3	0.4	1.5E−4	−25.0	0.0	0.15	−3.0E−6	−0.147	0.0

M	k	p_{ref}^c [kPa]	λ	β [1/kPa]	r	p^c [kPa]	ρ^T	p_o^* [kPa]
1.5	0.1	13.0	0.15	5.0E−5	0.75	100.0	0.2	1.4E+4

(b) Hydraulic properties

$g_{\alpha o}$ [1/m]	g_{no}	S_{res}^l	S_{sat}^l	ξ_n^T [1/K]	ξ_w^T [1/K]	K_{sat}^l [m/s]	K_{sat}^g [m/s]
12.0E−04	1.22	0.01	1.0	−1.0E−4	−1.5E−3	1.9E−14	0.2885

(c) Thermal properties

λ_{sat} [W/m/K]	λ_{dry} [W/m/K]	τ	f_{Tv}	c_s [J/kg/K]	c_w^l [J/kg/K]	c_w^g [J/kg/K]	c_a [J/kg/K]
1.15	0.47	0.8	1.0	1000.0	4180.0	1900.0	1000.0

(d) Phases properties

ρ_{wo}^l [kg/m^3]	β_{wp} [1/pa]	ρ^{so} [kg/m^3]	β_{sT} [1/K]	β_{wT} [1/K]
998.2	4.58E−10	2700.0	7.80E−6	2.10E−4

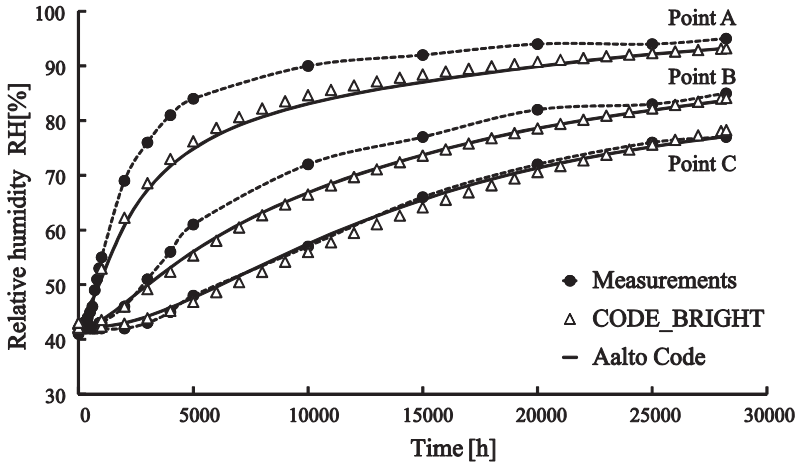

Fig. 12. Measured and calculated relative humidity in the case of isothermal infiltration.

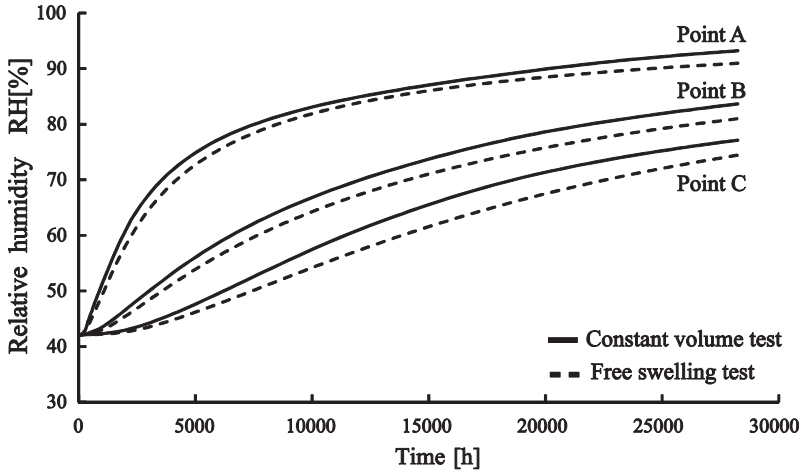

Fig. 13. A comparison showing the effect of mechanical boundary conditions on the calculated relative humidity.

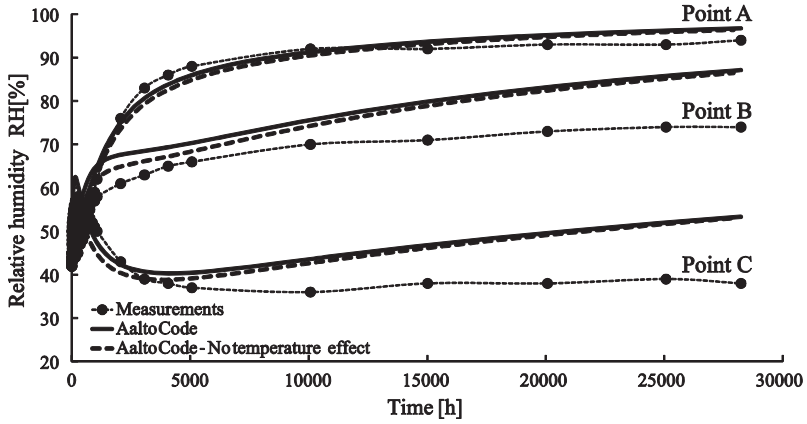

Fig. 14. Measured and calculated relative humidity in the case of non-isothermal infiltration. Both with and without considering the effect of temperature on the soil water retention curve.

$$\frac{\partial S^{l}_{abs}}{\partial t} = \alpha_{swell} S^{l} \tag{118}$$

In such a case, the results indicate noticeable improvement when adopting the previous formula for hydraulic conductivity with $\alpha_{swell} = 5.0 \times 10^{-9}$ (Fig. 16). The developed swelling pressure at point A is shown in Fig. 17. The slower hydration in case of the modified permeability resulted in a lower value for the predicted swelling pressure (considered equal to the vertical stress). Note that the calculated gas, vapour and dry air pressures are shown in Fig. 18 only for the first 1400 h of the test. This is due to the fact that these variables reach a steady state afterwards.

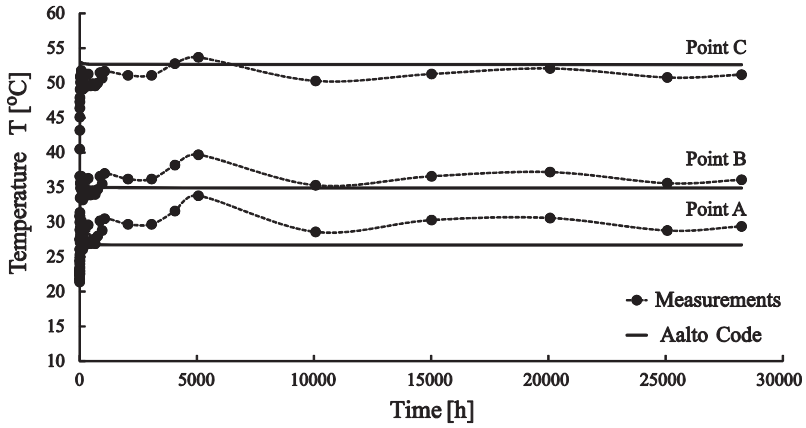

Fig. 15. The evolution of measured and calculated temperature in the case of non-isothermal infiltration.

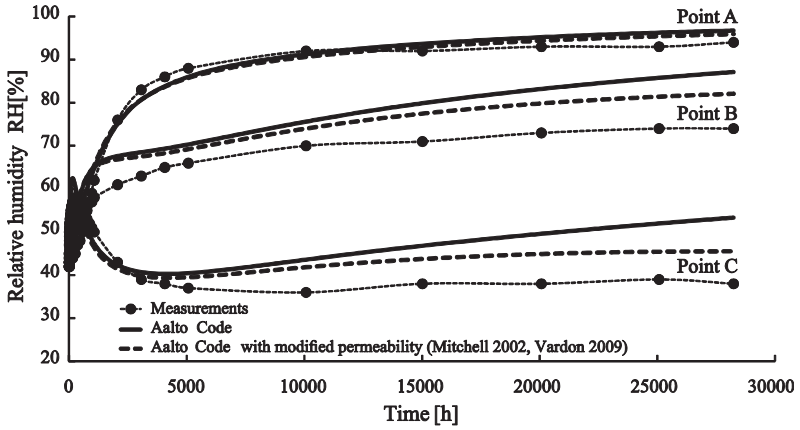

Fig. 16. Measured and calculated relative humidity evolution for the case of non-isothermal infiltration. Both with and without considering the effect of swelling on the water hydraulic conductivity.

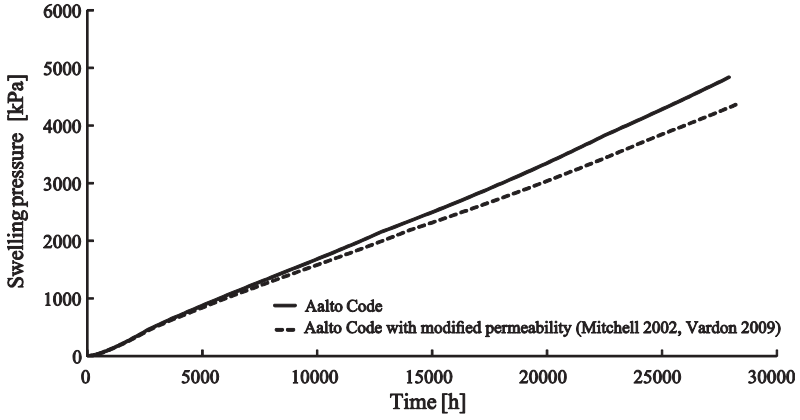

Fig. 17. Estimated swelling pressure at point A in the case of non-isothermal infiltration.

Fig. 18 shows that the total gas pressure remains around its initial atmospheric values for this particular test. This behaviour is attributed to the open gas flow boundary at the top of the sample and to the relatively high gas permeability used in this analysis.

4.4. Validation of coupled HM behaviour: infiltration test using MX80 bentonite

Marcial et al. [84] performed an infiltration test using MX80 bentonite under constant volume conditions. Full details about the experiment specifications are available in [84]. That test recorded the evolution of swelling pressure at different points of the sample over time providing excellent data to validate the numerical predictions, in particular with respect to hydro-mechanical coupling. The experiment employs an infiltration column of useful diameter and height of 0.05 m and 0.25 m, respectively. The MX80 bentonite in the column is compacted with 39 MPa compaction stress. The initial dry density is 1700 kg/m^3 at the initial gravimetric water content of 0.082 which corresponds to the initial suction of 103 MPa. The test is performed under

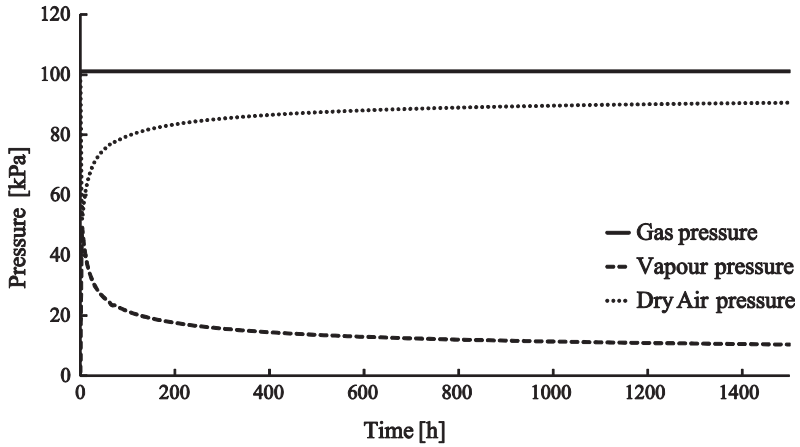

Fig. 18. Gas, water vapour, and dry air pressures at the lower end of the sample in the case of non-isothermal infiltration.

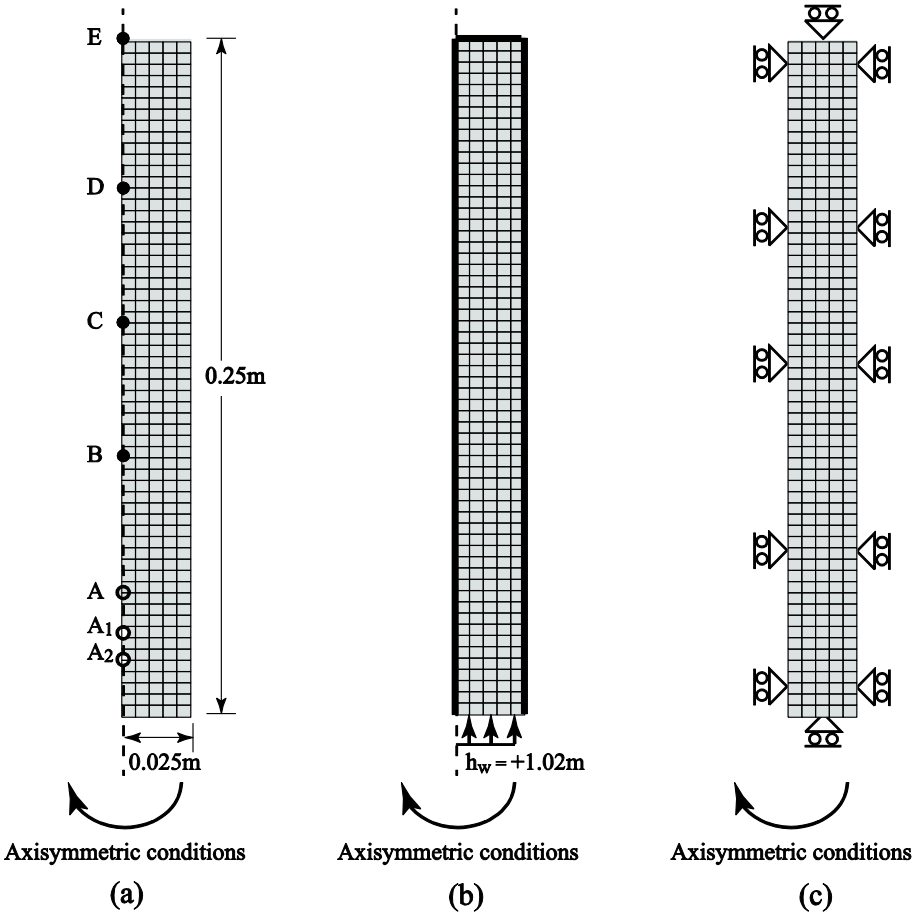

Fig. 19. Finite element model for MX80 infiltration test: (a) dimensions and control points locations; (b) hydraulic boundary conditions; (c) mechanical boundary conditions.

isothermal conditions with a constant temperature of 20 °C. In the experiment, the water, under pressure of 10 kPa, infiltrates the column from the base. Marcial et al. [84] recorded the evolution of swelling pressure (vertical stress) versus suction at several points along the column height (Point A at $z = 0.045$ m, Point A_1 at $z = 0.03$ m and Point A_2 at $z = 0.02$ m) (see Fig. 19(a)). The study also provided the relative humidity at specific locations (Point A at $z = 0.045$ m, Point B at $z = 0.095$ m, Point C at $z = 0.145$ m, Point D at $z = 0.195$ m and Point E at $z = 0.25$ m (see Fig. 19(a)). The total test duration is about 7.0 months (208 days).

4.4.1. Finite element model and material parameters

The finite element mesh consists of 300 quadrilateral 4-noded elements with four stress integration points per element as depicted in Fig. 19(a). The applied hydraulic and mechanical boundary conditions are shown in Fig. 19(b) and (c), respectively. A free initial stress state is assigned to the column model (minimum of 1.0 kPa). The bentonite is modelled as a BBM material (see Section 2.3.1) with the calibrated mechanical properties given in Table 4. The parameters of MX80 are kept in the same range to that provided in literature [55,85,86]. Eq. (92) estimates a value of

Table 4
MX80 bentonite properties as used in the infiltration test.

(a) Mechanical properties						
ν	κ_o	κ_{so}	n	α_k	α_{ks1}	α_{ks2}
0.3	0.03	0.3	0.4	−9.0E−6	−0.28	0.0
M	k	p^c_{ref} [kPa]	λ	β [1/kPa]	r	p^c [kPa]	p^*_o [kPa]
1.07	0.001	167.0	0.15	2.0E−5	0.8	100.0	10.6E+3
(b) Hydraulic properties						
$g_{\alpha o}$ [1/m]	g_{no}	g_{mo}	S^l_{res}	S^l_{sat}	K^l_{sat} [m/s]	α_{swell}
3.9E−04	1.65	0.5	0.0	1.0	1.0E−13	3.0E−8
(c) Phases properties						
ρ^l_{wo} [kg/m^3]			β_{wp} [1/pa]		ρ^{so} [kg/m^3]	
998.2			4.58E−10		2650.0	

about 10.6 MPa for the saturated preconsolidation pressure that matches the compaction pressure of 39 MPa at 103 MPa of suction. The extra BBM parameters that account for the expansive nature of MX80 bentonite are calibrated based on the provided experimental data and also listed in Table 4. The soil water retention data as given by [84,87,88] are fitted using the van Genuchten formula [23] with the parameters $g_{\alpha o} = 3.9\text{E}-4[1/\text{m}]$, $g_{no} = 1.65$, $g_{mo} = 0.5$, $S^l_{res} = 0.0$ and $S^l_{sat} = 1.0$ being graphically shown in Fig. 20. The bentonite relative permeability in the simulation follows Eq. (117) with $K^l_{sat} = 1.0 \times 10^{-13}$ m/s and calibrated $\alpha_{swell} = 3.0 \times 10^{-8}$. The saturated liquid water hydraulic conductivity is estimated based on the data provided by [84] and the experimental data by [26].

4.4.2. Discussion of numerical results

Fig. 21 shows reasonable agreement between the measured and calculated relative humidity at different locations of the column. This agreement again confirms the acceptable validity of the code for predicting the evolution of relative humidity. More interestingly, the relatively good agreement (at least qualitatively) between the calculated swelling pressure and the measurements as depicted in Fig. 22 gives more confidence about the potential behind the used approach. It is worth mentioning that predicting the evolution of swelling pressure is still one of the most challenging issues to model numerically. Even though it seems that the global behaviour can be captured satisfactorily qualitatively, the calibrated values are still considerably inaccurate and more research is still to be done for that aspect to be improved beside other issues. For example some further developments could incorporate thermal-osmotic flow, variations of the double-structure microstructure in both the mechanical and hydraulic behaviour of bentonite [76,82,88–92] and inclusion of simple chemical effects. The Aalto Code has been written in such a way that these extensions may be easily implemented.

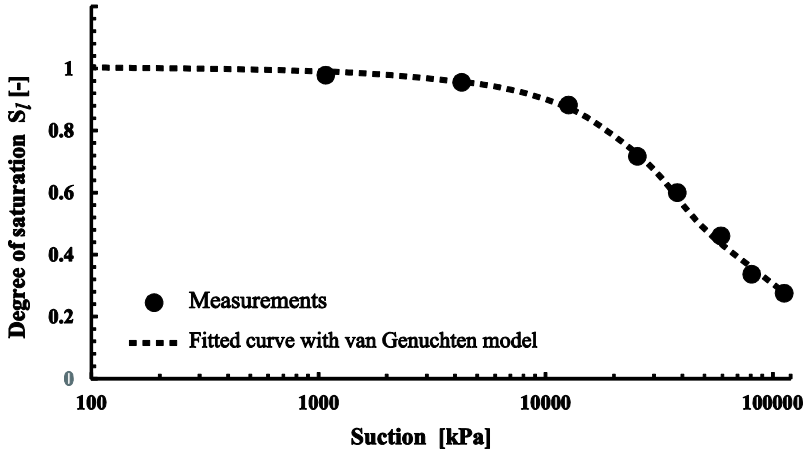

Fig. 20. Fitted soil water retention curve for MX80 bentonite.

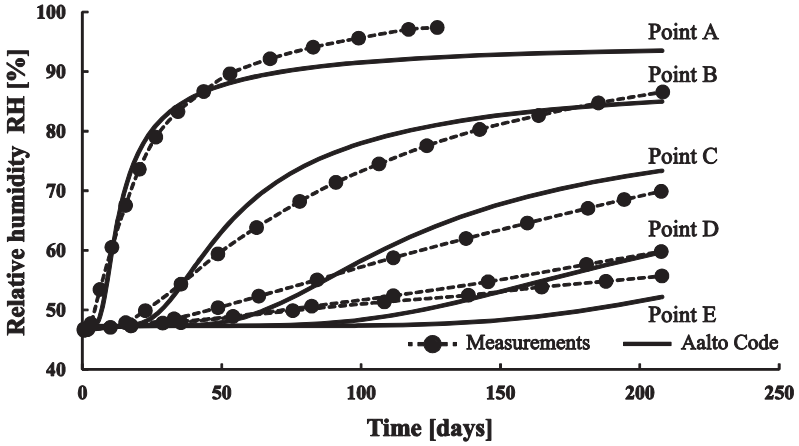

Fig. 21. Measured and calculated relative humidity at different points of the column.

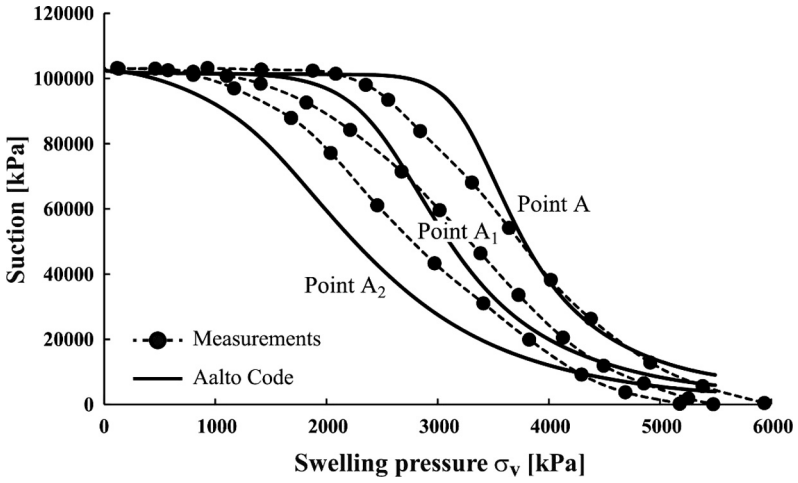

Fig. 22. Measured and calculated swelling pressure at different points of the column.

5. Conclusions

This paper presents a new finite element implementation of a newly proposed fully coupled thermo-hydro-mechanical framework. The detailed mathematical formulations of the governing equations for bentonite are discussed with an in-depth illustration of underlying assumptions. An extended version of the Barcelona Basic Model which incorporates thermal effects is reviewed along with a derivation of an explicit formula for the plastic multiplier. All information used for the finite element discretisation and implementation are explained and discussed in detail. The code performance has been verified by comparing its results to known analytical solutions for water infiltration and heat flow. The hydro-mechanical coupling has also been verified with results produced by the well-established CODE_BRIGHT thermo-hydro-mec hanically-coupled code. Finally, the code has been validated against experimental results for isothermal and non-isothermal infiltration. The verification and validation indicate that the code has been implemented correctly and may be used as a cornerstone for further developments. This may be in the form of additional chemical coupling, as well as an extension of the formulation via an improved hydraulic and mechanical constitutive model taking into account the microstructure effects, based on physically sound assumptions.

This paper clearly indicates the physical assumptions in the THM framework and is intended as a single 'how-to' reference for THM coupling in bentonite as well as unsaturated soils or porous materials in general.

Acknowledgment

The authors would like to gratefully acknowledge that the presented research has been funded by KYT2018 Finnish Research Programme on Nuclear Waste Management via THEBES project. Special thanks are due to Professor Antonio Gens from the Polytechnic University of Catalonia in Spain for providing the data for the CIEMAT infiltration tests and to Dr. Mika Laitinen from Numerola Oy in Finland for his support during the numerical implementation of the code. The authors would also like to thank the anonymous reviewers of the paper for their very constructive comments.

Appendix A

The derivatives in formula (24) are given as follows:

$$\frac{\partial S^l}{\partial S^l_{so}} = \left[1 + (g_\alpha|\psi|)^{g_n}\right]^{g_m} \tag{A.1}$$

$$\frac{\partial S^l_{so}}{\partial T} = \xi^T_w \tag{A.2}$$

$$\frac{\partial S^l}{\partial g_\alpha} = g_m g_n |\psi| \left(S^l_{so} - S^l_{res}\right)(g_\alpha|\psi|)^{g_n-1}\left[1 + (g_\alpha|\psi|)^{g_n}\right]^{\frac{1}{g_n}-2} \tag{A.3}$$

$$\frac{\partial g_\alpha}{\partial T} = \frac{1.54\times 10^{-4}}{\sigma^t} g_\alpha \tag{A.4}$$

$$\frac{\partial S^l}{\partial g_n} = \left(S^l_{so} - S^l_{res}\right)\left(1 + (g_\alpha|\psi|)^{g_n}\right)^{g_m}\left[\frac{g_m \mathrm{Ln}(g_\alpha|\psi|)(g_\alpha|\psi|)^{g_n}}{1 + (g_\alpha|\psi|)^{g_n}} - \frac{\mathrm{Ln}\left(1 + (g_\alpha|\psi|)^{g_n}\right)}{g_n^2}\right] \tag{A.5}$$

$$\frac{\partial g_n}{\partial T} = \xi^T_n g^2_n \tag{A.6}$$

Appendix B

After transferring the strong formulation of the balance equations (49), (61), (71) and (73) into a weak integral formulation and then applying Galerkin's weighted residuals method [93–95] one gets the discretised form in the shape of system of coupled algebraic equations as shown in Eq. (102) where the equations coefficients are determined as follows:

$$\boldsymbol{M}_{uu} = \int_\Omega (\nabla \boldsymbol{N}_b)^T \boldsymbol{M} \nabla \boldsymbol{N}_b d\Omega \tag{B.1}$$

$$\boldsymbol{M}_{wu} = \begin{cases} 0.0, & \psi > 0 \\ \int_\Omega (\boldsymbol{N}_b)^T \rho^l_w g \boldsymbol{m}^T \nabla \boldsymbol{N}_b d\Omega, & \psi = 0 \end{cases} \tag{B.2}$$

$$\boldsymbol{M}_{gu} = \begin{cases} \int_\Omega (\boldsymbol{N}_b)^T \rho^l_w g \boldsymbol{m}^T \nabla \boldsymbol{N}_b d\Omega, & \psi > 0 \\ 0.0, & \psi = 0 \end{cases} \tag{B.3}$$

$$\boldsymbol{M}_{Tu} = 0.0 \tag{B.4}$$

$$\boldsymbol{M}_{uw} = \int_\Omega (\boldsymbol{N}_a)^T \left[S^l \rho^l_w + S^g \rho^g_w\right] \nabla \boldsymbol{N}_b d\Omega \tag{B.5}$$

$$\boldsymbol{M}_{ww} = \int_\Omega (\boldsymbol{N}_a)^T \left[n S^l \beta_{wp} g \rho^{l^2}_w + n S^g \frac{\rho^g_w g M_w}{RT} - n\left(\rho^l_w - \rho^g_w\right)\frac{\partial S^l}{\partial \psi}\right] \boldsymbol{N}_b d\Omega \tag{B.6}$$

$$\boldsymbol{M}_{gw} = \int_{\Omega} (\boldsymbol{N}_a)^T \left[n\left(\rho^l_w - \rho^g_w\right) \frac{\partial S^l}{\partial \psi} - nS^g \frac{\rho^g_w g M_w}{RT} \right] \boldsymbol{N}_b d\Omega \tag{B.7}$$

$$\boldsymbol{M}_{Tw} = \int_{\Omega} (\boldsymbol{N}_a)^T \left[n\left(\rho^l_w - \rho^g_w\right) \frac{\partial S^l}{\partial T} - (1-n)\left(S^l \rho^l_w + S^g \rho^g_w\right)\beta_{sT} \right.$$
$$\left. -nS^l \beta_{wT} \rho^l_w + nS^g \frac{\rho^g_w}{T^2}\left(4974 + \frac{gM_w\psi}{R}\right) \right] \boldsymbol{N}_b d\Omega \tag{B.8}$$

$$\boldsymbol{M}_{ug} = \int_{\Omega} (\boldsymbol{N}_a)^T \rho_a \left[S^g + HS^l\right] \nabla \boldsymbol{N}_b d\Omega \tag{B.9}$$

$$\boldsymbol{M}_{wg} = -\int_{\Omega} (\boldsymbol{N}_a)^T \left[n\left[S^g + HS^l\right] \frac{M_a}{M_w} \frac{\rho^g_w g M_w}{RT} + n\rho_a [H-1] \frac{\partial S^l}{\partial \psi} - n\rho_a S^l \frac{\partial H}{\partial h_w} \right] \boldsymbol{N}_b d\Omega \tag{B.10}$$

$$\boldsymbol{M}_{gg} = \int_{\Omega} (\boldsymbol{N}_a)^T \left[n\left[S^g + HS^l\right] \left(\frac{M_a \rho^l_w g}{RT} + \frac{M_a}{M_w} \frac{\rho^g_w g M_w}{RT} \right) + n\rho_a [H-1] \frac{\partial S^l}{\partial \psi} \right] \boldsymbol{N}_b d\Omega \tag{B.11}$$

$$\boldsymbol{M}_{Tg} = \int_{\Omega} (\boldsymbol{N}_a)^T \left[n\rho_a [H-1] \frac{\partial S^l}{\partial T} + n\rho_a S^l \frac{\partial H}{\partial T} - (1-n)\rho_a \left[S^g + HS^l\right] \beta_{sT} \right.$$
$$\left. -n\left[S^g + HS^l\right] \frac{M_a}{M_w} \frac{\rho^g_w}{T^2}\left(4974 + \frac{gM_w\psi}{R}\right) \right] \boldsymbol{N}_b d\Omega \tag{B.12}$$

$$\boldsymbol{M}_{uT} = \int_{\Omega} (\boldsymbol{N}_a)^T \left(A(1-n) + LS^g \rho^g_w\right) \nabla \boldsymbol{N}_b d\Omega \tag{B.13}$$

$$\boldsymbol{M}_{wT} = \int_{\Omega} (\boldsymbol{N}_a)^T \left[-n\left(C - L\rho^g_w\right) \frac{\partial S^l}{\partial \psi} - \left(n\left[HS^l c_a + S^g c_a\right](T - T_o) \right) \frac{M_a}{M_w} \frac{\rho^g_w g M_w}{RT} \right.$$
$$+ \left(\left[nS^l c^l_w \right](T - T_o) \right) \beta_{wp} g \rho^{l^2}_w$$
$$\left. + nS^g \left(c^g_w (T - T_o) + L\right) \frac{\rho^g_w g M_w}{RT} + nS^l \rho_a c_a (T - T_o) \frac{\partial H}{\partial h_w} \right] \boldsymbol{N}_b d\Omega \tag{B.14}$$

$$\boldsymbol{M}_{gT} = \int_{\Omega} (\boldsymbol{N}_a)^T \left[n\left(C - L\rho^g_w\right) \frac{\partial S^l}{\partial \psi} + \left(n\left[HS^l c_a + S^g c_a\right](T - T_o) \right) \right.$$
$$\left. \left(\frac{M_a \rho^l_w g}{RT} + \frac{M_a}{M_w} \frac{\rho^g_w g M_w}{RT} \right) - nS^g \left(c^g_w (T - T_o) + L\right) \frac{\rho^g_w g M_w}{RT} \right] \boldsymbol{N}_b d\Omega \tag{B.15}$$

$$\boldsymbol{M}_{TT} = \int_{\Omega} (\boldsymbol{N}_a)^T \left[nS^l \rho_a c_a (T - T_o) \frac{\partial H}{\partial T} + n\left(C - L\rho^g_w\right) \frac{\partial S^l}{\partial T} \right.$$
$$- \left[A + B + (1-n) LS^g \rho^g_w\right] \beta_{sT} + D - \left(n\left[HS^l c_a + S^g c_a\right](T - T_o) \right) \frac{M_a}{M_w} \frac{\rho^g_w}{T^2}$$
$$\left(4974 + \frac{gM_w\psi}{R}\right) + nS^g \left(c^g_w (T - T_o) + L\right) \left[\frac{\rho^g_w}{T^2}\left(4974.0 + \frac{gM_w\psi}{R}\right) \right]$$
$$\left. - \left(\left[nS^l c^l_w \right](T - T_o) \right) \beta_{wT} \rho^l_w \right.$$

$$\boldsymbol{K}_{uw} = 0.0 \tag{B.17}$$

$$\boldsymbol{K}_{ww} = \int_{\Omega} (\nabla \boldsymbol{N}_a)^T \rho^l_w \boldsymbol{K}_w \nabla \boldsymbol{N}_b d\Omega + \int_{\Omega} (\nabla \boldsymbol{N}_a)^T \boldsymbol{D}_{vw} \nabla \boldsymbol{N}_b d\Omega \tag{B.18}$$

$$\boldsymbol{K}_{gw} = \int_{\Omega} (\nabla \boldsymbol{N}_a)^T \rho^g_w \boldsymbol{K}_g \nabla \boldsymbol{N}_b d\Omega - \int_{\Omega} (\nabla \boldsymbol{N}_a)^T \boldsymbol{D}_{vw} \nabla \boldsymbol{N}_b d\Omega \tag{B.19}$$

$$\boldsymbol{K}_{Tw} = \int_{\Omega} (\nabla \boldsymbol{N}_a)^T \boldsymbol{D}_{vT} \nabla \boldsymbol{N}_b d\Omega \tag{B.20}$$

$$\boldsymbol{K}_{ug} = 0.0 \tag{B.21}$$

$$\boldsymbol{K}_{wg} = \int_{\Omega} (\nabla \boldsymbol{N}_a)^T \rho_a H \boldsymbol{K}_w \nabla \boldsymbol{N}_b d\Omega - \int_{\Omega} (\nabla \boldsymbol{N}_a)^T \boldsymbol{D}_{vw} \nabla \boldsymbol{N}_b d\Omega \tag{B.22}$$

$$\boldsymbol{K}_{gg} = \int_{\Omega} (\nabla \boldsymbol{N}_a)^T \rho_a \boldsymbol{K}_g \nabla \boldsymbol{N}_b d\Omega + \int_{\Omega} (\nabla \boldsymbol{N}_a)^T \boldsymbol{D}_{vw} \nabla \boldsymbol{N}_b d\Omega \tag{B.23}$$

$$\boldsymbol{K}_{Tg} = -\int_{\Omega} (\nabla \boldsymbol{N}_a)^T \boldsymbol{D}_{vT} \nabla \boldsymbol{N}_b d\Omega \tag{B.24}$$

$$\boldsymbol{K}_{uT} = 0.0 \tag{B.25}$$

$$\boldsymbol{K}_{wT} = \left[\left(\rho^l_w c^l_w + \rho_a c_a H\right)(T - T_o) \right] \int_{\Omega} (\nabla \boldsymbol{N}_a)^T \boldsymbol{K}_w \nabla \boldsymbol{N}_b d\Omega$$
$$+ \left[\left(c_a - c^g_w\right)(T - T_o) + L \right] \int_{\Omega} (\nabla \boldsymbol{N}_a)^T \boldsymbol{D}_{vw} \nabla \boldsymbol{N}_b d\Omega \tag{B.26}$$

$$\boldsymbol{K}_{gT} = \left[\left(\rho_a c_a + \rho^g_w c^g_w\right)(T - T_o) + L\rho^g_w \right] \int_{\Omega} (\nabla \boldsymbol{N}_a)^T \boldsymbol{K}_g \nabla \boldsymbol{N}_b d\Omega$$
$$- \left[\left(c_a - c^g_w\right)(T - T_o) + L \right] \int_{\Omega} (\nabla \boldsymbol{N}_a)^T \boldsymbol{D}_{vw} \nabla \boldsymbol{N}_b d\Omega \tag{B.27}$$

$$\boldsymbol{K}_{TT} = \int_{\Omega} (\nabla \boldsymbol{N}_a)^T \lambda_T \nabla \boldsymbol{N}_b d\Omega - \left[\left(c_a - c^g_w\right)(T - T_o) + L \right]$$
$$\int_{\Omega} (\nabla \boldsymbol{N}_a)^T \boldsymbol{D}_{vT} \nabla \boldsymbol{N}_b d\Omega - (\boldsymbol{N}_a)^T \left[\left(\rho_a c_a + \rho^g_w c^g_w\right) \boldsymbol{q}^g + \left(\rho^l_w c^l_w + \rho_a c_a H\right) \boldsymbol{q}^l \right.$$
$$\left. + \left(c_a - c^g_w\right) \boldsymbol{j}^g_w \right] \int_{\Omega} \nabla \boldsymbol{N}_b d\Omega \tag{B.28}$$

$$\delta \boldsymbol{f}_u = \int_{\Omega} \delta \boldsymbol{b} \boldsymbol{N}_b d\Omega + \int_{\Gamma} \delta \boldsymbol{t} \boldsymbol{N}_b d\Gamma \tag{B.29}$$

$$\boldsymbol{f}_w = -\int_{\Omega} \rho^l_w \boldsymbol{K}_w \nabla \boldsymbol{N}_a d\Omega + \int_{\Gamma} (\boldsymbol{N}_a)^T \widehat{\boldsymbol{q}}_{ww} d\Gamma - \int_{\Omega} \rho^g_w \boldsymbol{K}_g \nabla \boldsymbol{N}_a$$
$$\times \frac{\rho^g}{\rho^l_w} d\Omega + \int_{\Gamma} (\boldsymbol{N}_a)^T \widehat{\boldsymbol{q}}_{wg} d\Gamma + \int_{\Gamma} (\boldsymbol{N}_a)^T \widehat{\boldsymbol{q}}_{vw} d\Gamma$$
$$- \int_{\Gamma} (\boldsymbol{N}_a)^T \widehat{\boldsymbol{q}}_{vg} d\Gamma + \int_{\Gamma} (\boldsymbol{N}_a)^T \widehat{\boldsymbol{q}}_{vT} d\Gamma \tag{B.30}$$

$$\boldsymbol{f}_g = -\int_{\Omega} \rho_a \boldsymbol{K}_g \nabla \boldsymbol{N}_a \frac{\rho^g}{\rho^l_w} d\Omega + \int_{\Gamma} (\boldsymbol{N}_a)^T \widehat{\boldsymbol{q}}_{gg} d\Gamma$$
$$- \int_{\Omega} \rho_a H \boldsymbol{K}_w \nabla \boldsymbol{N}_a d\Omega + \int_{\Gamma} (\boldsymbol{N}_a)^T \widehat{\boldsymbol{q}}_{gw} d\Gamma$$
$$- \int_{\Gamma} (\boldsymbol{N}_a)^T \widehat{\boldsymbol{q}}_{vw} d\Gamma + \int_{\Gamma} (\boldsymbol{N}_a)^T \widehat{\boldsymbol{q}}_{vg} d\Gamma - \int_{\Gamma} (\boldsymbol{N}_a)^T \widehat{\boldsymbol{q}}_{vT} d\Gamma \tag{B.31}$$

$$\boldsymbol{f}_T$$
$$= \int_{\Gamma} (\boldsymbol{N}_a)^T \widehat{\boldsymbol{q}}_T d\Gamma - \left[\left(\rho_a c_a + \rho^g_w c^g_w\right)(T - T_o) + L\rho^g_w \right]$$
$$\left(\int_{\Omega} \boldsymbol{K}_g \nabla \boldsymbol{N}_a \frac{\rho^g}{\rho^l_w} d\Omega - \int_{\Gamma} (\boldsymbol{N}_a)^T \widehat{\boldsymbol{q}}_{Tg} d\Gamma \right)$$
$$- \left[\left(\rho^l_w c^l_w + \rho_a c_a H\right)(T - T_o) \right] \left(\int_{\Omega} \boldsymbol{K}_w \nabla \boldsymbol{N}_a d\Omega - \int_{\Gamma} (\boldsymbol{N}_a)^T \widehat{\boldsymbol{q}}_{Tw} d\Gamma \right)$$
$$+ \left[\left(c_a - c^g_w\right)(T - T_o) + L \right] \left(\int_{\Gamma} (\boldsymbol{N}_a)^T \widehat{\boldsymbol{q}}_{vw} d\Gamma - \int_{\Gamma} (\boldsymbol{N}_a)^T \widehat{\boldsymbol{q}}_{vg} d\Gamma \right.$$
$$\left. + \int_{\Gamma} (\boldsymbol{N}_a)^T \widehat{\boldsymbol{q}}_{vT} d\Gamma \right) \tag{B.32}$$

with

$$A = \left[-\rho^s c_s + HS^l \rho_a c_a + S^g \rho_a c_a + S^l \rho^l_w c^l_w + S^g \rho^g_w c^g_w \right](T - T_o)$$

$$B = [(1-n)\rho^s c_s](T - T_o)$$

$$C = \left[H\rho_a c_a - \rho_a c_a + \rho^l_w c^l_w - \rho^g_w c^g_w \right](T - T_o)$$

$$D = n\left[HS^l\rho_a c_a + S^g\rho_a c_a + S^l\rho_w^l c_w^l + S^g\rho_w^g c_w^g\right] + (1-n)\rho^s c_s$$

$$\widehat{\boldsymbol{q}}_{ww} = \rho_w^l \boldsymbol{K}_w\left(\nabla \boldsymbol{N}_b \widehat{\boldsymbol{h}}_w + 1\right)\boldsymbol{n}$$

$$\widehat{\boldsymbol{q}}_{wg} = \rho_w^g \boldsymbol{K}_g\left(\nabla \boldsymbol{N}_b \widehat{\boldsymbol{h}}_g + \frac{\rho^g}{\rho_w^l}\right)\boldsymbol{n}$$

$$\widehat{\boldsymbol{q}}_{vw} = \boldsymbol{D}_{vw}\nabla \boldsymbol{N}_b \widehat{\boldsymbol{h}}_w \boldsymbol{n}$$

$$\widehat{\boldsymbol{q}}_{vg} = \boldsymbol{D}_{vw}\nabla \boldsymbol{N}_b \widehat{\boldsymbol{h}}_g \boldsymbol{n}$$

$$\widehat{\boldsymbol{q}}_{vT} = \boldsymbol{D}_{vT}\nabla \boldsymbol{N}_b \widehat{\boldsymbol{T}}\boldsymbol{n}$$

$$\widehat{\boldsymbol{q}}_{gg} = \rho_a \boldsymbol{K}_g\left(\nabla \boldsymbol{N}_b \widehat{\boldsymbol{h}}_g + \frac{\rho^g}{\rho_w^l}\right)\boldsymbol{n}$$

$$\widehat{\boldsymbol{q}}_{gw} = \rho_a H\boldsymbol{K}_w\left(\nabla \boldsymbol{N}_b \widehat{\boldsymbol{h}}_w + 1\right)\boldsymbol{n}$$

$$\widehat{\boldsymbol{q}}_{T} = \lambda_T \nabla \boldsymbol{N}_b \widehat{\boldsymbol{T}}\boldsymbol{n}$$

$$\widehat{\boldsymbol{q}}_{Tg} = \boldsymbol{K}_g\left(\nabla \boldsymbol{N}_b \widehat{\boldsymbol{h}}_g + \frac{\rho^g}{\rho_w^l}\right)\boldsymbol{n}$$

$$\widehat{\boldsymbol{q}}_{Tw} = H\boldsymbol{K}_w\left(\nabla \boldsymbol{N}_b \widehat{\boldsymbol{h}}_w + 1\right)\boldsymbol{n}$$

The normal vector on the domain boundaries is $\boldsymbol{n}$ whereas $\widehat{\boldsymbol{q}}$ represents a boundary flux vector. The symbols $\boldsymbol{N}_a$ and $\boldsymbol{N}_b$ represent the basis and the element shape functions, respectively.

References

[1] Chapman N, McCombie C. Principles and standards for the disposal of long-lived radioactive wastes. Elsevier; 2003.
[2] Nagasaki S, Nakayama S. Radioactive waste engineering and management. Springer; 2015.
[3] Olivella S, Gens A, Carrera J, Alonso E. Numerical formulation for a simulator (CODE_BRIGHT) for the coupled analysis of saline media. Eng Comput 1996;13:87–112.
[4] Thomas H, He Y. A coupled heat–moisture transfer theory for deformable unsaturated soil and its algorithmic implementation. Int J Numer Meth Eng 1997;40:3421–41.
[5] Seetharam S, Thomas H, Cleall P. Coupled thermo/hydro/chemical/mechanical model for unsaturated soils—numerical algorithm. Int J Numer Meth Eng 2007;70:1480–511.
[6] Laloui L, Klubertanz G, Vulliet L. Solid–liquid–air coupling in multiphase porous media. Int J Numer Anal Meth Geomech 2003;27:183–206.
[7] Rutqvist J, Börgesson L, Chijimatsu M, Kobayashi A, Jing L, Nguyen T, et al. Thermohydromechanics of partially saturated geological media: governing equations and formulation of four finite element models. Int J Rock Mech Min Sci 2001;38:105–27.
[8] Schrefler BA, Zhan X, Simoni L. A coupled model for water flow, airflow and heat flow in deformable porous media. Int J Numer Meth Heat Fluid Flow 1995;5:531–47.
[9] Alonso EE, Gens A, Josa A. A constitutive model for partially saturated soils. Géotechnique 1990;40:405–30.
[10] Gens A. Constitutive laws. Springer; 1995.
[11] CODE-BRIGHT U. A 3D program for thermo-hydro-mechanical analysis in geological media, user's guide. UPC [S.l.]; 2002.
[12] Laloui L, Nuth M, Vulliet L. Experimental and numerical investigations of the behaviour of a heat exchanger pile. Int J Numer Anal Meth Geomech 2006;30:763–81.
[13] Akrouch GA, Sánchez M, Briaud J. Thermo-mechanical behavior of energy piles in high plasticity clays. Acta Geotech 2014;9:399–412.
[14] Nishimura S, Gens A, Olivella S, Jardine R. THM-coupled finite element analysis of frozen soil: formulation and application. Geotechnique 2009;59:159.
[15] Viggiani G. Coupled phenomena induced by freezing in a granular material. Multilevel Model Secure Syst QoP-ML 2015:467.
[16] Olivella S, Carrera J, Gens A, Alonso E. Nonisothermal multiphase flow of brine and gas through saline media. Transp Porous Media 1994;15:271–93.
[17] Panday S, Corapcioglu MY. Reservoir transport equations by compositional approach. Transp Porous Media 1989;4:369–93.
[18] Diersch H, Kolditz O. Variable-density flow and transport in porous media: approaches and challenges. Adv Water Resour 2002;25:899–944.
[19] Verruijt A. Computational geomechanics. Springer Science & Business Media; 1995.
[20] Jacinto AC, Villar MV, Gómez-Espina R, Ledesma A. Adaptation of the van Genuchten expression to the effects of temperature and density for compacted bentonites. Appl Clay Sci 2009;42:575–82.
[21] Jacinto A, Villar M, Ledesma A. Influence of water density on the water-retention curve of expansive clays. Geotechnique 2012;62:657–67.
[22] Leong EC, Rahardjo H. Review of soil-water characteristic curve equations. J Geotech Geoenviron Eng 1997;123:1106–17.
[23] Van Genuchten MT. A closed-form equation for predicting the hydraulic conductivity of unsaturated soils. Soil Sci Soc Am J 1980;44:892–8.
[24] Leong EC, Rahardjo H. Permeability functions for unsaturated soils. J Geotech Geoenviron Eng 1997;123:1118–26.
[25] Börgesson L, Hernelind J. Preliminary modelling of the water saturation phase of the buffer and backfill materials. International progress report IPR-00-11; 1999.
[26] Villar M. MX-80 bentonite, thermo-hydro-mechanical characterisation performed at CIEMAT in the context of the prototype project. Informes Técnicos Ciemat 2005;1053:39.
[27] Villar M, Sánchez M, Gens A. Behaviour of a bentonite barrier in the laboratory: experimental results up to 8years and numerical simulation. Phys Chem Earth, Parts A/B/C 2008;33:S476–85.
[28] Van Esch JM. Adaptive multiscale finite element method for subsurface flow simulation. TU Delft: Delft University of Technology; 2010.
[29] Villar Galicia M. Thermo-hydro-mechanical characterisation of a bentonite from Cabo de Gata A study applied to the use of bentonite as sealing material in high level radioactive waste repositories. Publicación técnica. (Empresa Nacional de Residuos Radiactivos); 2002. p. 15–258.
[30] Bear J. Dynamics of fluids in porous media. Courier Corporation; 2013.
[31] Olivella S, Carrera J, Gens A, Alonso E. Porosity variations in saline media caused by temperature gradients coupled to multiphase flow and dissolution/precipitation. Transp Porous Media 1996;25:1–25.
[32] Wang W, Kosakowski G, Kolditz O. A parallel finite element scheme for thermo-hydro-mechanical (THM) coupled problems in porous media. Comput Geosci 2009;35:1631–41.
[33] Philip J, De Vries D. Moisture movement in porous materials under temperature gradients. Eos, Trans Am Geophys Union 1957;38:222–32.
[34] De Vries DA. The theory of heat and moisture transfer in porous media revisited. Int J Heat Mass Transf 1987;30:1343–50.
[35] Cleall PJ, Singh RM, Thomas HR. Vapour transfer in unsaturated compacted bentonite. Géotechnique 2013;63:957–64.
[36] Ewen J, Thomas H. Heating unsaturated medium sand. Geotechnique 1989;39:455–70.
[37] Ho CK, Webb SW. Gas transport in porous media. Springer; 2006.
[38] Yang D, Rahardjo H, Leong EC, Choa V. Coupled model for heat, moisture, air flow, and deformation problems in unsaturated soils. J Eng Mech 1998;124:1331–8.
[39] Vaunat J, Jommi C, Gens A. A strategy for numerical analysis of the transition between saturated and unsaturated flow conditions 1997:297–302.
[40] Itälä A, Olin M. Chemical evolution of bentonite buffer in a final repository of spent nuclear fuel during the thermal phase. Nucl Technol 2011;174:342–52.
[41] Collin F, Li X, Radu J, Charlier R. Thermo-hydro-mechanical coupling in clay barriers. Eng Geol 2002;64:179–93.
[42] Wang W, Rutqvist J, Görke U, Birkholzer JT, Kolditz O. Non-isothermal flow in low permeable porous media: a comparison of Richards' and two-phase flow approaches. Environ Earth Sci 2011;62:1197–207.
[43] Fung Y. Foundations of solid mechanics. Prentice Hall; 1965.
[44] Zienkiewicz OC, Taylor RL, Taylor RL. The finite element method. McGraw-hill London; 1977.
[45] Gens A, Jouanna P, Schrefler B. MODERN ISSUES IN NON-SATURATED SOILS 1995;.
[46] Hueckel T, Baldi G. Thermoplasticity of saturated clays: experimental constitutive study. J Geotech Eng 1990;116:1778–96.
[47] François B, Laloui L. ACMEG-TS: a constitutive model for unsaturated soils under non-isothermal conditions. Int J Numer Anal Meth Geomech 2008;32:1955–88.
[48] Abed AA, Vermeer PA. Numerical simulation of unsaturated soil behaviour. Int J Comput Appl Technol 2009;34:2–12.
[49] Abed AA. Numerical modeling of expansive soil behavior PhD thesis. Stuttgart University; 2008.
[50] Borja RI, Lee SR. Cam-clay plasticity, part 1: implicit integration of elasto-plastic constitutive relations. Comput Methods Appl Mech Eng 1990;78:49–72.
[51] Sołowski WT, Gallipoli D. Explicit stress integration with error control for the Barcelona basic model: Part I: Algorithms formulations. Comput Geotech 2010;37:59–67.
[52] Sołowski WT, Hofmann M, Hofstetter G, Sheng D, Sloan SW. A comparative study of stress integration methods for the Barcelona basic model. Comput Geotech 2012;44:22–33.
[53] Sloan SW, Abbo AJ, Sheng D. Refined explicit integration of elastoplastic models with automatic error control. Eng Comput 2001;18:121–94.
[54] Sheng D, Smith DW, Sloan S, Gens A. Finite element formulation and algorithms for unsaturated soils. Part II: Verification and application. Int J Numer Anal Meth Geomech 2003;27:767–90.

[55] Abed AA, Laitinen M, Lämsä J, Harjupatana T, Sołowski WT, Kataja M. Hydro-mechanical modelling of MX-80 bentonite: one dimensional study. E3S Web Conf 2016;9. EDP Sciences.
[56] Schofield A, Wroth P. Critical state soil mechanics; 1968.
[57] Gens A, Sánchez M, Sheng D. On constitutive modelling of unsaturated soils. Acta Geotech 2006;1:137.
[58] Wheeler S, Gallipoli D, Karstunen M. Comments on use of the Barcelona Basic Model for unsaturated soils. Int J Numer Anal Meth Geomech 2002;26:1561–71.
[59] Sołowski W, Sloan S. Equivalent stress approach in modelling unsaturated soils. Int J Numer Anal Meth Geomech 2012;36:1667–81.
[60] Sołowski W, Sloan S. Equivalent stress approach in creation of elastoplastic constitutive models for unsaturated soils. Int J Geomech 2013;15:04014041.
[61] Sánchez M, Gens A, Olivella S. THM analysis of a large-scale heating test incorporating material fabric changes. Int J Numer Anal Meth Geomech 2012;36:391–421.
[62] Haxaire A, Galavi V, Brinkgreve R. Definition and implementation of a fully coupled THM model for unsaturated rocks; 2013.
[63] Jaky J. Pressure in silos 1948;1:103–7.
[64] Laloui L, Cekerevac C. Thermo-plasticity of clays: an isotropic yield mechanism. Comput Geotech 2003;30:649–60.
[65] Wu W, Li X, Charlier R, Collin F. A thermo-hydro-mechanical constitutive model and its numerical modelling for unsaturated soils. Comput Geotech 2004;31:155–67.
[66] Haxaire A, Vardon PJ, Galavi V, Brinkgreve RB. Implementing a fully-coupled thermo-hydro-mechanical model: lessons learned from the application to radioactive waste storage; 2015.
[67] Kanno T, Kato K, Yamagata J. Moisture movement under a temperature gradient in highly compacted bentonite. Eng Geol 1996;41:287–300.
[68] Laitinen M. Numerrin 4.0 Manual. Numerola Oy: Jyväskylä; 2013.
[69] Galavi V. Groundwater flow, fully coupled flow deformation and undrained analyses in PLAXIS 2D and 3D; 2010.
[70] Johnson C. Numerical solution of partial differential equations by the finite element method. Courier Corporation; 2012.
[71] Srivastava R, Yeh TJ. Analytical solutions for one-dimensional, transient infiltration toward the water table in homogeneous and layered soils. Water Resour Res 1991;27:753–62.
[72] Van Wijk W, De Vries D. Periodic temperature variations. Phys Plant Environ 1963:133–8.
[73] Villar M, Gómez-Espina R. Report on thermo-hydro-mechanical laboratory tests performed by CIEMAT on FEBEX bentonite 2004–2008. Informes Técnicos CIEMAT; 2009. p. 1178.
[74] Villar M, Lloret A. Influence of temperature on the hydro-mechanical behaviour of a compacted bentonite. Appl Clay Sci 2004;26:337–50.
[75] Gens A, Zandarin MT. Report: Capabilities and requirements of numerical models 1/69; 2009.
[76] Vardon PJ. A three-dimensional numerical investigation of the thermo-hydro-mechanical behaviour of a large-scale prototype repository. Cardiff University; 2009.
[77] Sánchez M, Gens A, Villar MV, Olivella S. Fully coupled thermo-hydro-mechanical double-porosity formulation for unsaturated soils. Int J Geomech 2016;D4016015.
[78] Handbook P. DuPont™ Teflon® PTFE.
[79] Gens A, Sánchez M, Guimaraes LDN, Alonso E, Lloret A, Olivella S, et al. A full-scale in situ heating test for high-level nuclear waste disposal: observations, analysis and interpretation. Géotechnique 2009;59:377.
[80] Olivella S, Gens A. Vapour transport in low permeability unsaturated soils with capillary effects. Transp Porous Media 2000;40:219–41.
[81] Sánchez M, Arson C, Gens A, Aponte F. Analysis of unsaturated materials hydration incorporating the effect of thermo-osmotic flow. Geomech Energy Environ 2016.
[82] Mitchell HP. An investigation into the thermo/hydro/mechanical interactions involved in high level nuclear waste disposal; 2002.
[83] Thomas HR, Vardon PJ, Cleall PJ. Three-dimensional behaviour of a prototype radioactive waste repository in fractured granitic rock. Can Geotech J 2013;51:246–59.
[84] Marcial D, Delage P, Cui YJ. Hydromechanical couplings in confined MX80 bentonite during hydration; 2008.
[85] Toprak E, Mokni N, Olivella S, Pintado X. Thermo-hydro-mechanical modelling of buffer, synthesis report; 2013.
[86] Kristensson O, Åkesson M. Mechanical modeling of MX-80–quick tools for BBM parameter analysis. Phys Chem Earth, Parts A/B/C 2008;33:S508–15.
[87] Tang A, Cui Y, Barnel N. Compression-induced suction change in a compacted expansive clay 2008:369–74.
[88] Delage P, Marcial D, Cui Y, Ruiz X. Ageing effects in a compacted bentonite: a microstructure approach. Géotechnique 2006;56:291–304.
[89] Della Vecchia G, Dieudonné A, Jommi C, Charlier R. Accounting for evolving pore size distribution in water retention models for compacted clays. Int J Numer Anal Meth Geomech 2015;39:702–23.
[90] Romero E, Della Vecchia G, Jommi C. An insight into the water retention properties of compacted clayey soils. Géotechnique 2011;61:313–28.
[91] Lloret-Cabot M, Wheeler SJ, Sánchez M. A unified mechanical and retention model for saturated and unsaturated soil behaviour. Acta Geotechnica; 2017. p. 1–21.
[92] Tripathy S, Sridharan A, Schanz T. Swelling pressures of compacted bentonites from diffuse double layer theory. Can Geotech J 2004;41:437–50.
[93] Fish J, Belytschko T. A first course in finite elements. John Wiley & Sons; 2007.
[94] Hutton D. Fundamentals of finite element analysis. McGraw-Hill; 2004.
[95] Smith IM, Griffiths DV, Margetts L. Programming the finite element method. John Wiley & Sons; 2013.